UNIWERSYTET TECHNOLOGICZNO-PRZYRODNICZY
IM. JANA I JĘDRZEJA ŚNIADECKICH
W BYDGOSZCZY

ZESZYTY NAUKOWE NR 260

TELEKOMUNIKACJA I ELEKTRONIKA
15

WYDZIAŁ TELEKOMUNIKACJI
I ELEKTROTECHNIKI

BYDGOSZCZ – 2011

UNIWERSYTET TECHNOLOGICZNO-PRZYRODNICZY
IM. JANA I JĘDRZEJA ŚNIADECKICH
W BYDGOSZCZY

ZESZYTY NAUKOWE NR 260

TELEKOMUNIKACJA I ELEKTRONIKA 15

BYDGOSZCZ – 2011

ISSN 1899-0088

Wydawnictwa Uczelniane Uniwersytetu Technologiczno-Przyrodniczego
ul. Ks. A. Kordeckiego 20, 85-225 Bydgoszcz, tel. 52 3749482, 3749426
e-mail: wydawucz@utp.edu.pl http://www.wu.utp.edu.pl/

Wyd. I. Nakład 80 egz. Ark. aut. 3,1. Ark. druk. 3,9.
Zakład Małej Poligrafii UTP Bydgoszcz, ul. Ks. A. Kordeckiego 20

Contents

UNIWERSYTET TECHNOLOGICZNO-PRZYRODNICZY
IM. JANA I JĘDRZEJA ŚNIADECKICH W BYDGOSZCZY
ZESZYTY NAUKOWE NR 260
TELEKOMUNKACJA I ELEKTRONIKA 15 (2011), 5-17

INVARIANT GABOR-ZERNIKE DESCRIPTOR FOR POSTAL APPLICATIONS

Tomasz Andrysiak, Mirosław Miciak, Rafał Boniecki

Institute of Telecommunications,
Faculty of Telecommunications and Electrical Engineering
University of Technology and Life Sciences (UTP)
ul. Kaliskiego 7, 85-789 Bydgoszcz, Poland
[andrys, miciak, raboni]@utp.edu.pl

Summary: In this paper a new solution of handwritten digits recognition system for postal applications is presented. Moreover, in this paper, a new method of handwritten characters recognition is introduced. The proposed algorithm is applied to classification of post mails on the basis of zip code information. In connection with this work the research was conducted with numeric characters used in real post code of mail pieces. Moreover, the article contains basic image processing for instance filtration binarization and normalization of the character. The main objective of this article is to use the Gabor filtration and Zernike moments to obtain a set of invariant features, on basis of which postal code will be recognized. The reported experiments' results prove the effectiveness of the proposed method. Furthermore, sources of errors as well as possible improvement of classification results will be discussed.

Keywords: Character recognition, Gabor filters, Zernike moments.

1. INTRODUCTION

The today's systems of automatic sorting of the post mails use the OCR (Optical Character Recognition) mechanisms. In the present recognizing of addresses (particularly written by hand) the OCR is insufficient.

The typical system of sorting (Fig. 1) consists of the image acquisition unit, video coding unit and OCR unit. The image acquisition unit sends the mail piece image to the OCR for interpretation. If the OCR unit is able to provide the sort of information required (this technology has 50 % effectiveness for all mails [9], it sends this data to the sorting system, otherwise the image of the mail pieces is sent to the video coding unit, where the operator writes down the information about mail pieces.

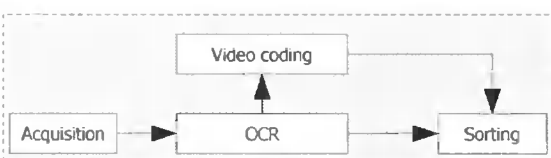

Fig. 1. The automatic sorting system – mail flow

The main problem is that operators of the video coding unit have lower throughput than an OCR and induce higher costs [9]. Therefore the OCR module is improving, particularly in the field of recognition of the characters. Although these satisfactory results were received for printed writing, the handwriting is still difficult to recognize. Taking into consideration the fact that manually described mail pieces make 30% of the whole mainstream, it is important to improve the possibility of segment recognizing of handwriting. This paper presents the proposal of a system for recognition of handwritten characters, for reading post code from mail pieces.

2. SYSTEM OVERVIEW

The process of character recognition process can be divided into stages: image grayscale normalization, filtration and binarization, normalization, Gabor and Zernike moments calculating, Principal Component Analysis, feature vector building, and character recognition stage. The first step of the image processing is image grayscale normalization. The colorful image most often represented by three coefficients: Red, Green and Blue (RGB) from the acquisition unit must be converted to the gray scale image. The next step of processing of the image of mail piece is digital filtration and binarization. The final stage of preprocessing is coordinate normalization. The proposed method of character recognition was shown on Fig. 2. Additionally, our solution proposed the use of the preliminary classification stage. The aim of the preliminary classification stage is to reduce the number of possible candidates for an unknown character, to a subset of the total character set. For this purpose, the selected domain is categorized into subgroups. The analysis of the elements belonging to different groups does not allow to indicate the clear membership rules classes of character, but rather may show their geometrical features. Additionally, pre-classification module can be used to determine rejection of non-digit character too. Based on the feature vector (G,E,Z) recognition, the classification attempts to identify the character based on the calculation of Euclidean distance between the features of the character and of the character models [2].

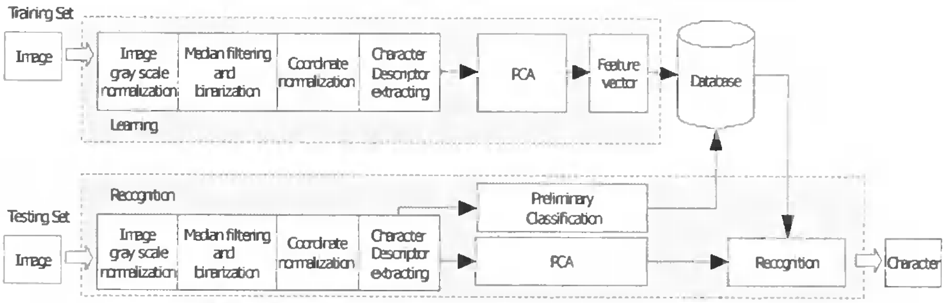

Fig. 2. The proposed method of character recognition

2.1. Image grayscale normalization

Before filtering the image, we normalize all its regions to a certain mean and variance. Normalization is performed to remove the effects of sensor noise and gray level deformation. Moreover, the extraction of salient points, performed later in our method, depends on the illumination variance in the image. Therefore, in order to achieve illumination and contrast invariance, we normalize the image [37].

Let $I(x,y)$ denote the gray value at the pixel (x,y), E and V be the estimated mean and illumination variance in the image I, respectively, and $I_n(x,y)$ stand for the normalized gray level value at the pixel (x,y).

For all the pixels in the image I, the normalization process is defined as follows [4,5]:

$$I_n(x,y) = \begin{cases} E_0 + \sqrt{\frac{V_0(I(x,y)-E)^2}{V}} & if\ I(x,y) > T_n, \\ E_0 - \sqrt{\frac{V_0(I(x,y)-E)^2}{V}} & otherwise, \end{cases} \tag{1}$$

here E_0 and V_0 are the desired mean and variance values, respectively, E and V are the computed mean and variance in the given image, described by

$$E = \frac{1}{MN}\sum_{x=0}^{M-1}\sum_{y=0}^{N-1} I(x,y), \tag{2}$$

$$V = \frac{1}{MN}\sum_{x=0}^{M-1}\sum_{y=0}^{N-1}(I(x,y) - E)^2, \tag{3}$$

respectively. In our case, $E_0 = 100$, $V_0 = 100$ and $T_n = 128$. In result of the operation of luminance levels normalization we obtain image I_n.

2.2. Median filtering and binarization

In the next step, we perform median filtering and binarization. The filtration is used for improving the quality of the image, emphasizing details and making processing of the image easier. The filtration of digital images is obtained by convolution operation. The new value of point of image is counted on the basis of neighboring points value. Every value is classified and it has influence on new value of point of the image after filtration. In the pre-processing part non-linear filtration was applied. The statistical filter separates the signal from the noise, but it does not destroy useful information. This is particularly important when applied to images that contain addresses data with salt and pepper noise coming from e.g. not uniform writing surfaces. The applied filter is median filter, with mask 3x3. After filtration the binarization stage is applied. Due to the use of images that contain mostly text, we decided to use the histogram-based thresholding method. These types of methods are very efficient when compared to other image segmentation methods because they typically require only one pass through the pixels. The histogram is computed from all of the pixels in the image, and the peaks and valleys in the histogram are used to locate the class in the image. However, the binary image is given by

$$I_b(x,y) = \begin{cases} 1 & if\ I_n(x,y) > T_b, \\ 0 & otherwise, \end{cases} \tag{4}$$

where T_b is a threshold value, such as the intensity of the first minimum that occurs after the maximum value of the intensity histogram. Additionally, this technique can be applied in recursive form, as the method to clusters in the image in order to divide them into smaller clusters. As result the binary stream of digit is received, which is sent to the next stage of processing.

Fig. 3. Images of the digits: from the preprocessing stage, after filtration and after binarization

2.3. Coordinate normalization

The image of character received from the acquisition stage have different distortion such as: translation, rotation and scaling. The character normalization is applied for standardization size of the character. Images there are translated, rotated and expanded or decreased. we change the $[x, y]$ coordinate system into an invariant system of $[x', y']$ coordinates such as

$$[x', y', 1] = \begin{bmatrix} 1 & 0 & 0 \\ 0 & 1 & 0 \\ -P & -Q & 1 \end{bmatrix} \times \begin{bmatrix} 1/\sigma_x & 0 & 0 \\ 0 & 1/\sigma_y & 0 \\ 0 & 0 & 1 \end{bmatrix} \times \begin{bmatrix} \cos\theta & \sin\theta & 0 \\ -\sin\theta & \cos\theta & 0 \\ 0 & 0 & 1 \end{bmatrix}. \qquad (5)$$

where

$$P = \frac{m_{10}}{m_{00}}, \qquad Q = \frac{m_{01}}{m_{00}}, \qquad (6)$$

$$\sigma_x = \sqrt{\frac{m_{20}}{m_{00}} - P}, \quad \sigma_y = \sqrt{\frac{m_{02}}{m_{00}} - Q}, \qquad (7)$$

for moments of order $k + l$ defined as

$$m_{k,l} = \sum_{x=0}^{M-1} \sum_{y=0}^{N-1} x^k y^l I_b(x, y). \qquad (8)$$

In reality, we haven't got these parameters starting right now, so we use new coordinate system where the center is equal to center of gravity of the character. The value of angle rotation is according to main axes of the image. The value of scale coefficient is calculated by mean value of variation of the character. So, the center of gravity of the character is a good candidate point of the center of image as a product of normalization stage.

3. FEATURE EXTRACTION FOR CHARACTER RECOGNICTION

Each character in the image is characterized by a given localized spatial frequency or a narrow range of dominant localized spatial frequencies that differ significantly from dominant frequencies of other character. Gabor filters encode the character images into multiple narrow frequency and orientation channels [8,13].

3.1. Gabor filters

The general functional of the two-dimensional Gabor filter family can be represented as a Gaussian function modulated by a complex sinusoidal signal. Specifically, a two dimensional Gabor filter $G(x, y)$ can be formulated as [11]:

$$G(x,y;\lambda,\theta_k)=g(x,y;\sigma)\exp\left(\frac{2\pi x_{\theta_k}}{\lambda}i\right) \tag{9}$$

and $g(x,y;\sigma)$ is a Gaussian function with form:

$$g(x,y;\sigma)=\frac{1}{\sqrt{2\pi\sigma^2}}\exp\left(-\frac{x_\theta^2+y_\theta^2}{2\sigma^2}\right), \tag{10}$$

where

$$x_{\theta_k}=x\cos\theta_k+ysix\theta_k, \tag{11}$$

$$y_\theta=-x\sin\theta_k+y\cos\theta_k$$

and σ is the standard deviation of the Gaussian envelope along the x and y dimensions, and λ and θ_k are the wavelength and orientation, respectively.

A rotation of the $x-y$ plane by an angle θ_k will result in a Gabor filter at orientation θ_k.

The θ_k is defined by

$$\theta_k=\frac{\pi}{n}(k-1),\quad k=1,2,\dots,n \quad n\in N, \tag{12}$$

where n denotes the number of orientations.

A particular Gabor elementary function can be used as the mother wavelet to generate a whole family of Gabor wavelets. Examples of a particular set of 2D Gabor wavelets are presented in Fig. 4.

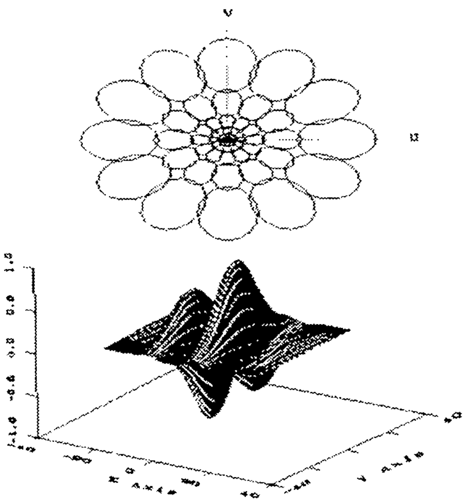

Fig. 4. Gabor Wavelets

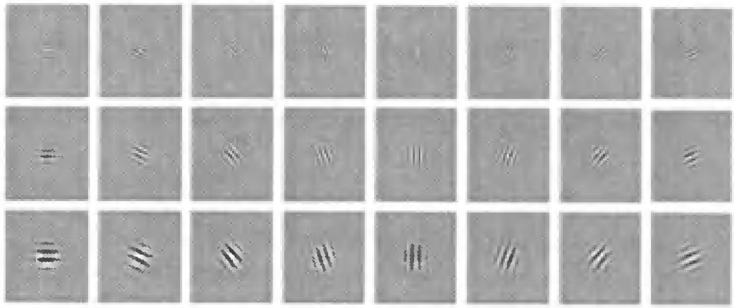

Fig. 5. The kernels of Gabor wavelets at three scales and eight orientations

The odd and even components of the above signal are as follows:

$$G_o\left(x,y;\lambda,\theta_k\right)=g\left(x,y\right)\cos\left(\frac{2\pi x_{\theta_k}}{\lambda}\right), \tag{13}$$

$$G_e\left(x,y;\lambda,\theta_k\right)=g\left(x,y\right)\sin\left(\frac{2\pi x_{\theta_k}}{\lambda}\right), \tag{14}$$

where G_e and G_o are the even-symmetric and odd-symmetric Gabor filters.

3.2. Gabor energy features extraction

The simplest idea to obtain other features than just filter responses is to apply a threshold to the Gabor filter results. The motivation for such an approach is the analogy to the function of simple cells which can be modeled by a linear weighted spatial summation, characterized by Gabor weighting functions and followed by a half-wave rectification [22].

The threshold Gabor features are computed as follows:

$$G_{T_o}\left(x,y;\sigma,\lambda,\theta_k\right)=\chi\left(G_o\left(x,y;\sigma,\lambda,\theta_k\right)\right), \tag{15}$$

$$G_{T_e}\left(x,y;\sigma,\lambda,\theta_k\right)=\chi\left(G_e\left(x,y;\sigma,\lambda,\theta_k\right)\right), \tag{16}$$

where

$$\chi\left(z\right)=\begin{cases}0 & for \quad z<0,\\ z & for \quad z\geq 0,\end{cases} \tag{17}$$

$G_o\left(x,y;\sigma,\lambda,\theta_k\right)$ and $G_e\left(x,y;\sigma,\lambda,\theta_k\right)$ are the odd and even components of Gabor filter responses, respectively.

The Gabor Energy feature is a combination of symmetric and asymmetric Gabor filter results. Gabor Energy is related to the model of a specific type of selective neuron orientation in the primary visual cortex called the complex cell [28]. Gabor Energy is given by

$$E(x,y;\sigma,\lambda,\theta_k)=\sqrt{G_{I_o}^2(x,y;\sigma,\lambda,\theta_k)+G_{I_e}^2(x,y;\sigma,\lambda,\theta_k)}, \tag{18}$$

where $G_{I_o}(x,y;\sigma,\lambda,\theta_k)$ and $G_{I_e}(x,y;\sigma,\lambda,\theta_k)$ are the threshold responses of the linear symmetric and asymmetric Gabor filters, respectively.

The Gabor Energy feature is also closely related to the local power spectrum. Local power spectrum features are obtained using the same filter bank as in the computations of Gabor Energy features:

$$P(x,y;\sigma,\lambda,\theta_k)=E^2(x,y;\sigma,\lambda,\theta_k). \tag{19}$$

3.3. Zernike moments of power spectrum

Zernike moments (ZM) are the projection of the power spectrum $P(x,y,\rho,\theta)$ on the orthogonal basis V_{pq}. The Zernike moments of order p with repetition q are defined as follows [32,36]:

$$ZM_{pq}=\frac{p+1}{\pi}\sum_{x=0}^{N-1}\sum_{y=0}^{N-1}P(x,y,\sigma,\lambda,\theta_k)V_{pq}^*(x,y). \tag{20}$$

The Zernike polynomials:

$$V_{pq}(x,y)=R_{pq}(\rho)\exp(jq\theta) \tag{21}$$

are a complete set of complex valued functions orthogonal on the unit disk D: $x^2+y^2\le 1$, where $p\ge 0$, and $p-|q|$ is even positive integer.

The polar coordinates (ρ,θ) in the image domain are related to the Cartesian coordinates (x,y) by:

$$\rho=\sqrt{x^2+y^2}\quad,\quad \theta=\arctan(y/x). \tag{22}$$

The Zernike polynomials $V_{pq}(x,y)$ are orthogonal basis set and satisfy the following condition:

$$\iint_D V_{pq}^*(x,y)V_{p'q'}(x,y)dxdy=\frac{\pi}{n+1}\delta_{pp'}\delta_{qq'}. \tag{23}$$

The radial polynomial $R_{pq}(\rho)$ is given by:

$$R_{pq}(\rho)=\sum_{l=0}^{(p-|q|)/2}F_{p|q|l}\,\rho^{p-2l}, \tag{24}$$

where

$$F_{p|q|l}=\frac{(-1)^l(p-l)!}{l!\left(\frac{p+|q|}{2}-l\right)!\left(\frac{p-|q|}{2}-l\right)!}. \tag{25}$$

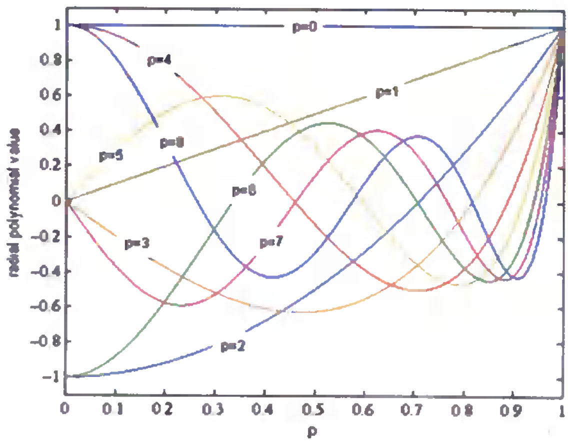

Fig. 6. Zernike polynomials of order $p = 0,1 \ldots 8$ and $q=0$ or 1

4. FEATURES VECTOR AND SIMILARITY MEASURE

After calculating Gabor features and Zernike moments, we obtain several feature vectors:

– the vector of even-symmetric and odd-symmetric Gabor filter responses

$$G = \left[G_o(x,y;\sigma,\lambda,\theta_k), G_e(x,y;\sigma,\lambda,\theta_k)\right], \tag{26}$$

– the vector of threshold and energy Gabor features given by

$$E = \left[G_{\Gamma_o}(x,y;\sigma,\lambda,\theta_k), G_{\Gamma_e}(x,y;\sigma,\lambda,\theta_k), E(x,y;\sigma,\lambda,\theta_k)\right], \tag{27}$$

– the vector of the Zernike moments of power spectrum

$$Z = \left[Z_1, Z_2, \ldots, Z_r, \ldots, Z_{c'}\right], \tag{28}$$

where

$$Z_r = \left\{\left|ZM_{pq}\right|, p \geq 0, p - |q| : even, p \geq q\right\} \tag{29}$$

and

$$r = \left\lfloor \frac{p}{2} \right\rfloor \left(\left\lfloor \frac{p}{2} + 1 \right\rfloor \right) + \left(\left\lfloor \frac{p}{2} + 1 \right\rfloor \right) \times \left(\left\lceil \frac{p}{2} \right\rceil - \left\lfloor \frac{p}{2} \right\rfloor \right) + \left(\left\lfloor \frac{q}{2} \right\rfloor \right), \tag{30}$$

where $\lceil a \rceil$ represents the largest integer that is not greater than a and $\lceil a \rceil$ denotes the smallest integer that is not smaller than a.

We calculate the similarity of a query image Q and an image D from the database, defined as

$$d^{(Q)(D)}(G,E,Z)=\sum_i\left[\frac{\left|G_i^{(Q)}-G_i^{(D)}\right|}{\sigma_G}+\frac{\left|E_i^{(Q)}-E_i^{(D)}\right|}{\sigma_E}+\frac{\left|Z_i^{(Q)}-Z_i^{(D)}\right|}{\sigma_Z}\right], \tag{31}$$

where i is the number of the extracted features and σ_G, σ_E, σ_Z are standard deviations of vector features G, E and Z over the entire database, respectively.

5. EXPERIMENTAL RESULTS

In this section we present the results of classification with proposed method. Especially for evaluation experiments, we extracted some digit data from various paper documents from different sources e.g. mail pieces post code, bank checks, etc. The character samples were scanned with 600 dpi in color and stored in special data collections [12] in form 24 bit RGB and 8 bit grayscale images. It is important that in the case of images with heterogeneous background to perform directional filtering for 0, 45 and 90 degrees. Character image is normalized according to specification of the second paragraph. Based on geometric and central moments, center of gravity and main axis angle can be achieved. For experimental purposes, the character image sizes are ranged from 32x32, 64x64, 128x128 to 256x256 pixels. Similar scenario was carried out for grayscale levels, where 2,4,8,16,32 and 64 levels were tested. In total, the datasets contain the digit patterns of above 150 writers. In this way were collected about 1400 different patterns for training and testing sets.

In our solution, we use odd and even component pairs of Gabor filters with the quadrature phase relationship. Each pair of the Gabor filters is tuned to a specific band of spatial frequency and orientation. There are some important points to note in selecting the channel parameters σ, λ and θ_k. Four values of orientation are used: 0, π/8, π/4, 3π/8, π/2, 5π/8, 3π/4, 7π/8. In our experiments for each orientation we select three spatial frequencies. This gives a total of 24 Gabor channels (8 orientations combined with 3 frequencies) [13,19].

The Principal Component Analysis module in proposal system generate a set of data, which can be used as features in building feature vector stage shown on Fig. 2. For instance when we use input features from Gabor features and Zernike moments calculation stage (GEZ) calculation stage, as a result we obtained 18 values vector, using Cattell's criterion [17]. Thus the use of PCA method [14,17,29] made it possible to reduce the dimensionality of classification vectors. For proposed method, after reducing the dimensions of the vector space of 120 features (GEZ) up to 20 in the prepared application to more than 3 times shorter test sets classification. It turned out that the reduction of classification vectors affected the effectiveness of the classification method used (31). where the characteristics were obtained for the 120 efficiency level of 96.2%, while after reduction to 16 features were obtained 97.9 % of correctly classified characters from our database. The best results were obtained for the GEZ character feature vector using $d^{(Q)(D)}(G,E,Z)$ similarity measurement. The results obtained for testing 5 sets defined in ratio 3:7 of all samples (testing set/learning set).

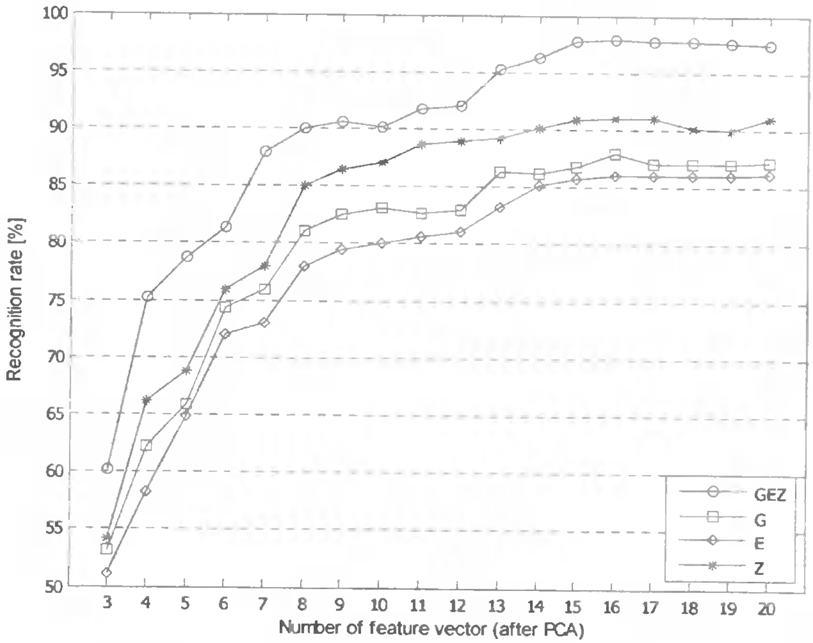

Fig. 7. Recognition rate for our database characters using features: G, E, Z, and GEZ

6. SUMMARY

The article presents an approach to optical character recognition, specifically used in the recognition of zip code digits. Although, the area is well known and explored, with successful examples of both scientific and commercial implementation, however efficiency of mail sorting systems is imperfect. The author hopes that this solution may be supportive for the previous works [24,25,26] and other approaches such as [2,6,15,21]. The most common optical character recognition methods are based on modified quadratic discriminant function, hidden Markov models, normalized Fourier descriptors, MLP-SVM.

In the article, we presented the idea and implementation of use of the Gabor filtration and Zernike moments in the process of character recognition in postal applications. In order to optimalize those procedures, in the first stage we prepared the pre-processing character image using gray scale and coordinate normalization, and median filtering.

In the article, approach to the optical character recognition was presented and tested. In our method, we performed the estimation of character features using Gabor filter responses equation (26), energy Gabor features (27) and Zernike moments of power spectrum (28). The second approach was based on the joined features GEZ (31). After experiments we concluded that Zernike features (Z) and energy Gabor features (E) were the most appropriate for character descriptor, respectively. Better results were achieved by GEZ features.

The main advantages of the method are: finding geometric relations of the character by our method, invariance to background noise, low computational complexity, working with grayscale images. Disadvantages: low value of the rejections, unclear data reduction from PCA, need to use preprocessing. Further work will include Rough Sets theory upgraded to all alphanumerical signs.

BIBLIOGRAPHY

[1] Arif T., Shaaban Z., Krekor L., Baba S., 2005. Object Classification via Geometrical, Zernike and Legendre Moments, Journal of Theoretical and Applied Information Technology, vol. 7, no. 1, pp. 31-37.

[2] Aissaoui A., 1999. Normalised Fourier Coefficients for Cursive Arabic Script recognition, Universite Mohamed, Morocco.

[3] Andrysiak T., Choraś M., 2003. Hierarchical object recognition using Gabor wavelets. Proc. Comput. Recogn. Syst., KOSYR, Miłków, Poland, pp. 271-278.

[4] Andrysiak T., Choraś M., 2005. Image Retrieval Based on Hierarchical Gabor Filters, International Journal Applied Mathematics and Computer Science (AMCS), vol. 15, no. 4, pp. 101-110.

[5] Andrysiak T., 2001. Recognition of handwritten characteres using Gabor features, II Krajowa Konferencja Naukowo-Szkoleniowa KOSYR.

[6] Bellili A., Giloux M., 2003. An MLP-SVM combination architecture for handwritten digit recognition. International Journal on Document Analysis and Recognition, Springer-Verlag.

[7] Choraś R., Andrysiak T., 1995. Gabor transforms in image processing, Proceedings of Signal Processing, Chapter Circuits and Systems, Poland Section IEEE, pp. 31-34.

[8] Choraś R., Andrysiak T., Śrótek M., 2001. Zastosowanie funkcji Gabora w przetwarzaniu, analizie i rozpoznawaniu obrazów, II Krajowa Konferencja Naukowo-Szkoleniowa KOSYR.

[9] 2000Forella G.,. Word perfect, Postal Technology. UKIP Media & Events Ltd. UK.

[10] Fluseer J., Zitova B., T. Suk, 2009. Moments and Moment Invariants in Pattern Recognition, Wiley Knowledge For Generations.

[11] Gabor D., 1946. Theory of communication, Journal Institute of Electrical Engineers, vol. 93, no. 26, pp. 429-457.

[12] Horstmann C.S., Cornell G., 2002. Core Java 2-Advanced Features, Sun micreosystems Press A Prentice Hall Title.

[13] Jain A., Ratha N., Lakshmanan S., 1997. Object detection using Gabor filters. Pattern Recognition, Vol. 30, No 2, pp. 295-309.

[14] Jolliffe I.T., 2002: Principal Component Analysis, Springer Series in Statistics, 2nd ed., Springer.

[15] Kaufmann G., Bunke H., 2000. Automated Reading of Cheque Amounts, Pattern Analysis & Applications, Springer-Verlag.

[16] Khotanzad A., 1990. Invariant Image Recognition by Zernike Moments, IEEE Transactions on Pattern Analysis and Machine Intelligence, vol. 12, no. 5, pp. 920--930.

[17] Kim K., 2003. Face Recognition using Principle Component Analysis, DCS, University of Maryland.
[18] Ledesma R.D., 2007. Determining the Number of Factors to Retain in EFA: an easy-to-use computer program for carrying out Parallel Analysis, PAR&E, vol. 12.
[19] Lee T.S., 1996. Image representation using 2D Gabor Wavelets, IEEE Transactions on Pattern Analysis and Machine Intelligence, vol. 18, no. 10, pp. 959-971.
[20] Liao S.X., Pawlak M., 1996. On image analysis by moments. IEEE Transactions on Pattern Analysis and Machine Intelligence, vol. 18, pp. 254–266.
[21] Liu C., Sako H., 2002. Performance evaluation of pattern classifiers for handwritten character recognition, International Journal on Document Analysis and Recognition, Springer-Verlag.
[22] Marcelja S., 1980. Mathematical description of the responses of simple cortical cells, Journal of the Optical Society of America, vol. 2(7), pp. 1297-1300.
[23] Mehrotra R., Namuduri K.R., Ranganathan N., 1992. Gabor filter – based edge detection, Pattern Recognition, vol. 25, no. 12, pp. 1479-1494.
[24] Miciak M., 2004. The Algorithms of Handwritten Characters Recognition For Postal Application, Signal Processing 2004 Workshop Proceedings, pp. 75-79.
[25] Miciak M., Maszewski M., 2007. Character Recognition Based on Fourier Transfrom and CDWT in Postal Applications, Advances in Soft Computing 45. Computer Recognition Systems 2, pp. 462-469, Springer.
[26] Miciak M., R. Boniecki, A. Marchewka, 2010. The Complex System to Postal Code Recognition. IPoCC 2010, Position of Postal Services in Modern Communication Society. pp. 216-221, Pardubice.
[27] Mukundan R., 2004. Some Computational Aspects of Discrete Orthogonal Moments, IEEE Transactions on Image Processing, vol. 13, no. 8, pp. 1055-1059.
[28] Porat M., Zeevi Y.Y, 1988. The generalized Gabor scheme of image representation in biological and machine vision, IEEE Transactions on Pattern Analysis and Machine Intelligence, Vol. 10, No 4, pp. 452-468.
[29] Shlens J., 2005. A Tutorial on Principal Component Analysis, available at: www.cs.princeton.edu/picasso/mats/PCA-Tutorial-Intuition_jp.pdf
[30] Smith L.I. A Tutorial on Principal Components Analyzing – Discusion and singular value decomposition, available at: www.cs.otago.ac.nz/cosc453/student_tutorials/principal_components.pdf
[31] Su Y.M., Wang J.F., 2003. A novel stroke extraction method for Chinese characters using Gabor filters, Pattern Recognition, vol. 36, no. 3, pp. 635-647.
[32] Sun-Kyoo H., Whoi-Yul K., 2006. A novel approach to the fast computation of Zernike moments, Pattern Recognition vol. 39, pp. 2065-2076.
[33] Teague M.R., 1998. Image Analysis Via the General Theory of Moments, Opt. Soc. Amer., vol. 70, pp. 920-930.
[34] Teague M.R., 1980. Image analysis via the general theory of moments. IEEE Transactions on Pattern Analysis and Machine Intelligence, vol. 70, no. 8. pp. 920-930.
[35] Teh Ch., Chin R.T., 1998. On Image Analysis by the Methods of Moments, IEEE Transactions on Pattern Analysis and Machine Intelligence, vol. 10, no. 4. pp. 496-512.

[36] Wallin A., 1995. Complete sets of complex Zernike moment invariants and the role of pseudo invariants, IEEE Transactions on Pattern Analysis and Machine Intelligence, vol. 17, pp. 1106-1110.

[37] Il Kang H., Lim S., Il Kim K., Ik Son Y., 2005. A Normalization Based Image Affine Estimation Technique for Computer Vision, Proceedings of the 2005 IEEE/ASME International Conference on Advanced Intelligent Mechatronics, pp. 1553-1556.

INWARIANTNY DESKRYPTOR GABORA-ZERNIKA DLA ZASTOSOWAŃ POCZTOWYCH

Streszczenie

W artykule przedstawiono nowe rozwiązanie zadania rozpoznawania znaków pisanych ręcznie dla zastosowań pocztowych. Zaproponowano algorytm klasyfikacji przesyłek pocztowych działający na podstawie informacji zawartej w zapisie kodu pocztowego. Ponadto w artykule opisano podstawowe operacje przetwarzania wstępnego tj. filtrację, binaryzację oraz normalizację obrazu znaku. Głównym nacisk położono na wykorzystanie filtracji Gabora i momentów Zernike do uzyskania zbioru cech na podstawie których rozpoznawano kod pocztowy. Otrzymane wyniki eksperymentów pozwoliły wykazać skuteczność proponowanej metody. Dodatkowo w pracy przedstawiono źródła potencjalnych błędów w procesie rozpoznawania, jak również zaproponowano możliwości poprawy wyników klasyfikacji.

Słowa kluczowe: rozpoznawanie znaków, filtracja Gabora, momenty Zernika

UNIWERSYTET TECHNOLOGICZNO-PRZYRODNICZY
IM. JANA I JĘDRZEJA ŚNIADECKICH W BYDGOSZCZY
ZESZYTY NAUKOWE NR 260
TELEKOMUNKACJA I ELEKTRONIKA 15 (2011), 19-35

PETRI NET MODELS OF DISCRETE EVENT SYSTEMS AND STATE SEQUENCE GENERATION FOR CLOSED LOOP PLANT-CONTROLLER SYSTEM

Wiesław Zech[1], Tadeusz Puchałka[2]

[1]University of Technology and Life Sciences
Kaliskiego 7, 85-789 Bydgoszcz, Poland
wieslaw.zech@utp.edu.pl

[2]Poznań University of Technology
Piotrowo 3A, 60-965 Poznań, Poland
tadeusz.puchalka@put.poznan.pl

Summary: In this paper there has been provided a ladder diagram formal model as LD-P/T-system. Closed loop system which consists of the LD-controller model and the controlled object model is constructed. We propose an algorithm to construct a state-transition diagram of the system. A fault is detected when an unpredicted state is generated. Additional benefits from such an approach results in the fact that an abstraction of the transition diagram of this controller is possible, which can be used for LD-VHDL transformation into FPGA implementation.

Keywords: DES, Petri nets, PLC, ladder diagram

1. INTRODUCTION

Examples of Discrete Event System (DES) can be found in automated production. In such a system, programmable logic controllers (PLCs) have been widely used. Programming languages for PLC are standardized (IEC 61131-3 2003). Ladder diagram (LD) is one of them and is very popular. Several approaches have been proposed [5, 7, 12] for fault detection in a sequential control system. In this paper a ladder diagram formal model is provided as LD-P/T-system. Closed loop system which consists of the LD-controller model and controlled object model is constructed. We propose an algorithm to construct a state-transition diagram of the system. A fault is detected when an unpredicted state is generated. Additional benefits from such an approach results in the fact that an abstraction of the transition diagram of this controller is possible, which can be used for LD-VHDL transformation into FPGA implementation [4].

This article is structured as follows: section 2 presents some background on Petri net, and provides formal models: some class of DES as I-P/N-system, B-system, section 3 is devoted to the brief description of LD, in section 4 we define LD-P/T-system and model of closed loop system (controller-plant). Algorithms are printed in the appendix.

2. PETRI NETS

Petri nets are a mathematical and graphical tool that can find application in many fields of science and engineering. Their characteristic feature is the ability of modeling the concurrency. The occurrence actions, under some conditions, is a natural phenomenon due to which Petri nets are perceived as a formal tool for modeling discrete event systems (DES) [6].

Definition 1.[10]

A. Petri net is a 3-tuple PN = (P, T, F), where:

$P = \{p_1, p_2, ..., p_m\}$ is a finite set of places,

$T = \{t_1, t_2, ..., t_n\}$ is a finite set of transitions,

$F: (P \times T) \cup (T \times P) \rightarrow \{0,1\}$ is a flow function

The following conditions are met:

(i) $P \cap T = \emptyset$,

(ii) $P \cup T \neq \emptyset$,

(iii) $\forall x \in P \cup T, \exists y \in P \cup T: F(x, y) \neq 0 \vee F(y, x) \neq 0$.

B. For PN = (P, T, F) $^{\bullet}t = \{p \in P \mid F(p, t) = 1\}$, $t^{\bullet} = \{p \in P \mid F(t, p) = 1\}$ are pre-places set, post-places set of $t \in T$, respectively.

$^{\bullet}p = \{t \in T \mid F(t, p) = 1\}$, $p^{\bullet} = \{t \in T \mid F(p, t) = 1\}$ are pre-transitions set, post-transitions set of $p \in P$, respectively.

C. PN = (P, T, F) is simple if $\forall x, y \in P \cup T: (^{\bullet}x = {}^{\bullet}y \wedge x^{\bullet} = y^{\bullet}) \Rightarrow x = y$.

In this paper only simple Petri nets have been considered.

Remark 1. Suitable form to describe PN is: PN = $\{t: (^{\bullet}t, t^{\bullet}) \mid \text{for } t \in T\}$

Definition 2.

A. [10] Marking of Petri net PN = (P, T, F) is mapping $m: P \rightarrow \mathbb{N}$ (or $m \in \mathbb{N}^P$), where $\mathbb{N} = \{0, 1, 2, ...\}$.

B. P/T-system is 3-tuple PS = (PN, δ, m_0), where: PN = (P, T, F) is Petri net, $m_0 \in \mathbb{N}^P \setminus \{\underline{0}\}$ is a initial marking (where $\forall p \in P: \underline{0}(p) = 0$). $\delta: \mathbb{N}^P \times T \longrightarrow \mathbb{N}^P$ is a partial function which describes behavior of PS so, that:

$\forall(m, t) \in dom.\delta : \delta(m, t) = (m - {}^{\bullet}\underline{t}) + \underline{t}^{\bullet}$, where

$$^{\bullet}\underline{t}: P \rightarrow \{0,1\},\ ^{\bullet}\underline{t}(p) = \begin{cases} 1, p \in {}^{\bullet}t \\ 0, p \notin {}^{\bullet}t \end{cases},\ \underline{t}^{\bullet}: P \rightarrow \{0,1\}, \underline{t}^{\bullet}(p) = \begin{cases} 1, p \in t^{\bullet} \\ 0, p \notin t^{\bullet} \end{cases}.$$

$dom.\delta = \{ (m, t) \in \mathbb{N}^P \times T \mid {}^{\bullet}\underline{t} \leq m \}$.

C. (notation)

- $\forall t \in T: {}^{\bullet\bullet}t = \{m \in M \mid (m, t) \in dom.\delta\}$,
- $\forall t \in T: t^{\bullet\bullet} = \{m \in M \mid \exists m' \in {}^{\bullet\bullet}t: m = \delta(m', t)\}$,
- $\forall m \in M: {}^{\bullet\bullet}m = \{t \in T \mid m \in t^{\bullet\bullet}\}$,
- $\forall m \in M: m^{\bullet\bullet} = \{t \in T \mid m \in {}^{\bullet\bullet}t\}$,
- $\forall m \in M:]m[_P = \{p \in P \mid m(p) \geq 1\}$.

Definition 3. [10] For every P/T-system PS = (P, T, F, δ, m_0) set M of reachable markings is defined as a minimal set, so that:

(i) $m_0 \in M$,

(ii) $\forall m' \in \mathbb{N}^P: \forall t \in T: [((m', t) \in dom.\delta \wedge m' \in M) \Rightarrow \delta(m', t) \in M]$.

Definition 4. [10, 6] P/T-system PS = (P, T, F, δ, m_0) is called safe iff
$\forall m \in M: \forall p \in P: m(p) \leq 1$.
Only safe P/T-systems are used in this work.

Definition 5. TSP = (M, T, Δ, m_0) is T(PS)-system generated by P/T-system
PS = (P, T, F, δ, m_0) if
(i) M is a set of reachable markings of PS,
(ii) T is a set of transitions of PS,
(iii) $\Delta = \{(m, t, m') \in M \times T \times M \mid T \cap (m^{\bullet\bullet} \cap {}^{\bullet\bullet}m') \neq \emptyset\}$,
(iv) m_0 is initial marking of PS.
An example of T(PS)-system is shown as follows in Fig. 1b.

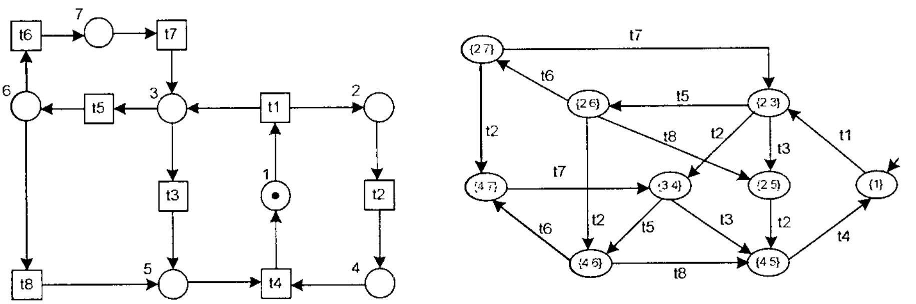

Fig. 1. Graphical representation of P/T-system PS = (PN, δ, m_0) with initial marking indicated as a dot placed at place 1,where PN = {t1: ({1},{2,3}), t2: ({2},{4}), t3: ({3},{5}), t4: ({4,5},{1}), t5: ({3},{6}), t6: ({6},{7}), t7: ({7},{3})} (a) and T(PS)- system generated by PS, where states (markings) are describe as sets of marked places (resp. to Def. 2.C) (b)

Theorem 1. [13] Every T(PS)-system PS = (P, T, F, δ, m_0) generated by P/T-system is a transition system in the sense of [8, 2, 3].
For this reason, T is being considered as a set of events, M as a set of states and Δ as a set of transition between states. It is assumed that events in the system can be enabled or disabled. It is a result of the internal system structure. P/T-system is fulfilling this role. Nevertheless, this inner behavior can be subjected to the influence of outside events and generates changes in the environment.

Definition 6. Interpreted P/T-system (I-P/T-system) is a 7-tuple IPS = (PS, XB, YB, LX, LY, ∂, Λ), where PS = (P, T, F, δ, m_0) is a P/T-system, $XB = \{0,1\}^X$, $YB = \{0,1\}^Y$ are function sets describing appropriately the states of input signals $X = \{x_1, x_2, \dots, x_n\}$, and output signals $Y = \{y_1, y_2, \dots, y_k\}$. The set values of output signals Y is expanded to set {0,1,-},where - is 'don't-care' symbol[1], than $YB^- = \{0,1,-\}^Y$ is an expanded set of states of output signals.
LX: $T \rightarrow FB(X \times \{0, 1\})$ is a labeling function of transitions, where for every $t \in T$: LX(t) is a boolean formula which consists of variables $(x, i) \in X \times \{0,1\}$ and logical operators: and, or.

[1] IEEE std 1164 for VHDL. [11]

LY: $P \to \{a \subseteq Y\times\{0,1\} \mid \exists u\in YB: a \subseteq \bar{\bar{u}}\}$ is a labeling function of places such that $\forall m \in M, \exists u \in YB: \bigcup_{p\in]m[_P} LY(p) \subseteq \bar{\bar{u}}$, where: M is a set of reachable markings of PS, $\bar{\bar{u}} = \{(y, i) \in Y\times\{0, 1\} \mid i = u(y)\}$, $]m[_P = \{p \in P \mid m(p) \neq 0\}$
Function $\hat{c} : M \times XB \to 2^M$ is an external transition of IPS. The value of $\hat{c}$ is being calculated according to the pattern: $\forall(m, w) \in M \times XB$:

$$\hat{c}(m, w) = \begin{cases} \{\underline{\delta}(m, sel(m, w))\}, & \text{if } stepTest(sel(m, w)) = True \\ \bigcup_{\tau \in \max(2^{sel(m,w)} \cap step(m))} \{\underline{\delta}(m, \tau)\}, & \text{if } \begin{cases} sel(m, w) \neq \emptyset \wedge \\ stepTest(sel(m, w)) = False \end{cases} \\ \{m\}, & \text{if } sel(m, w) = \emptyset \end{cases}$$

Case of the non-deterministic behavior for (m, w) occurs, when:
$sel(m, w) \neq \emptyset \wedge stepTest(sel(m, w)) = False$, where: sel: $M \times XB \to 2^T$, $sel(m, w) = SEL(w) \cap m^{\bullet\bullet}$, SEL: $XB \to 2^T$, $SEL(w) = \{t\in T \mid EVAL(w, LX(t)) = True\}$.
EVAL: $XB \times FB(X \times \{0,1\}) \to \{True, False\}$ is a function which evaluates labels of transitions. The value of EVAL is calculated according to formula:

$$EVAL(w, fb) = \begin{cases} True, & \text{if } fb = (\ ) \\ ev(w, fb), & \text{if } fb \in X \times \{0,1\} \cup \{True, False\} \\ EV(EVAL(w, fb1), EVAL(w, fb2), op), & \text{if others} \end{cases}$$

EV: $(\{True, False\}^2) \times Lop \to \{True, False\}$, $EV((val, val'), op) = val\ op\ val'$
ev: $XB \times ((X \times \{0,1\}) \cup \{True, False\}) \to \{True, False\}$,

$$ev(w, fb) = \begin{cases} True, \text{if } fb \in X \times \{0,1\} \wedge fb = (x, i) \wedge w(x) = i \\ False, \text{if } fb \in X \times \{0,1\} \wedge fb = (x, i) \wedge w(x) \neq i \\ fb, \text{if } fb \in \{True, False\} \end{cases}$$

, where $Lop = \{and, or\}$
$\max(2^{sel(m,w)} \cap step(m)) = \{\tau\in 2^{sel(m,w)} \cap step(m) \mid \forall\tau'\in 2^{sel(m,w)} \cap step(m): \tau \subseteq \tau' \Rightarrow \tau = \tau'\}$, stepTest: $2^{sel(m,w)} \to \{True, False\}$,

$$\forall\tau \in 2^{sel(m,w)}: stepTest(\tau) = \begin{cases} True, & \text{if } \forall(t, t') \in \tau \times \tau: ({}^{\bullet}t \cap {}^{\bullet}t' = \emptyset) \\ False, & \text{else} \end{cases}$$

$\underline{\delta}: M \times STEP(PS) \to M, \underline{\delta}(m, \tau) = (M - \sum_{t\in\tau} {}^{\bullet}\underline{t}) + \sum_{t\in\tau} \underline{t}^{\bullet}$
$STEP(PS) = \bigcup_{m\in M} step(m)$
$step(m) = \{\tau \in 2^T \mid \tau \subseteq m^{\bullet\bullet} \wedge stepTest(\tau) = True\}$ Optional: $\underline{\delta}':]M[\times STEP(PS) \to]M[, \underline{\delta}'(]m[_P, \tau) = (]m[_P \setminus pre(\tau)) \cup post(\tau)$, where: $pre(\tau) = \bigcup_{t\in\tau} {}^{\bullet}t, post(\tau) = \bigcup_{t\in\tau} t^{\bullet}$, $]M[= \{]m[_P \mid m \in M\}$ $\Lambda: M \to YB^-$ is an output function of IPS. The value of Λ is being calculated according to the formula:
$\forall m\in M, \forall y\in Y: \Lambda(m) = \Lambda'(m) \cup \{(y, -) \mid y \in Y \wedge \{(y, 0), (y, 1)\} \cap \Lambda'(m) = \emptyset\}$, where $\Lambda'(m) = \bigcup_{p\in]m[_P} LY(p)$.

Discrete values of signals X and Y can be expanded according to the needs, like in Definition 6: from {0, 1} to {0, 1, -}. Example of I-P/T-system is presented in Fig. 2.

Definition 7. $A(IPS) = (M, XB, YB^-, \partial, \Lambda, m_0)$ is a Moore automaton generated by I-P/T-system $IPS = (PS, XB, YB, LX, LY, \hat{c}, \Lambda)$. A(IPS) describes the behavior of IPS.

The behavior of IPS is deterministic if A(IPS) is deterministic, non-deterministic otherwise. The A(IPS) which is deterministic is a special case defined automata. In many applications. it is essential to make sure that the considered system is deterministic. So there is a need to make sure that the modeled system possesses this property. Diagram of Moore automaton generated by I-P/T-system specified in Fig. 2 is shown in Fig. 3.

In Definition 8 there is presented a new kind of the P/T-system, named B-system which is used for modeling ladder diagrams.

Remark 2. (notation) For every $w' \in XB$ and every $a \subseteq w'$: $\langle a \rangle = \{w \in XB \mid a \subseteq w'\}$. For example, if $a = \{(3,0), (4,1)\}$, than $\langle a \rangle = \{ \{(1,0), (2,0), (3,0), (4,1)\}, \{(1,0), (2,1), (3,0), (4,1)\}, \{(1,1), (2,0), (3,0), (4,1)\}, \{(1,1), (2,1), (3,0), (4,1)\} \}$, where $X = \{1, 2, 3, 4\}$. A shorter representation of the $w \in XB$ is possible. For example, the tuple $w' = (0, 1, 0, 1)$ is representing of $w = \{(1,0), (2,1), (3,0), (4,1)\}$, at the condition: $(i, w(i)) = (i, w'[i-1])$. or if $(x_i, w(x_i)) \in XB$, $(x_i, w(x_i)) = (x_i, w'[i-1])$

Definition 8. [13] B-system is a pair $BS = (PS, \eta)$ with a P/T-system $PS = (P, T, F, \delta, m_0)$ and bijection η: $P^0 \to P^1$, where $\{P^0, P^1\}$ is a partition of P. For η seen as relation $\eta \subseteq P^0 \times P^1$ the following conditions are met: (i) $\forall (p_j^0, p_j^1) \in \eta: |\{p_j^0, p_j^1\} \cap {}^\bullet t| = \forall (p_j^0, p_j^1) \in \eta: |\{p_j^0, p_j^1\} \cap t^\bullet| \leq 1$ (ii) $\forall (p_j^0, p_j^1) \in \eta: |\{p_j^0, p_j^1\} \cap]m_0[_P| = 1$

Definition 9. [10] For given P/T-system $PS = (P, T, F, \delta, m_0)$ set $P' \subseteq P$ is called P-invariant iff $\forall m \in M: \sum_{p \in P'} m(p) = \sum_{p \in P'} m_0(p)$

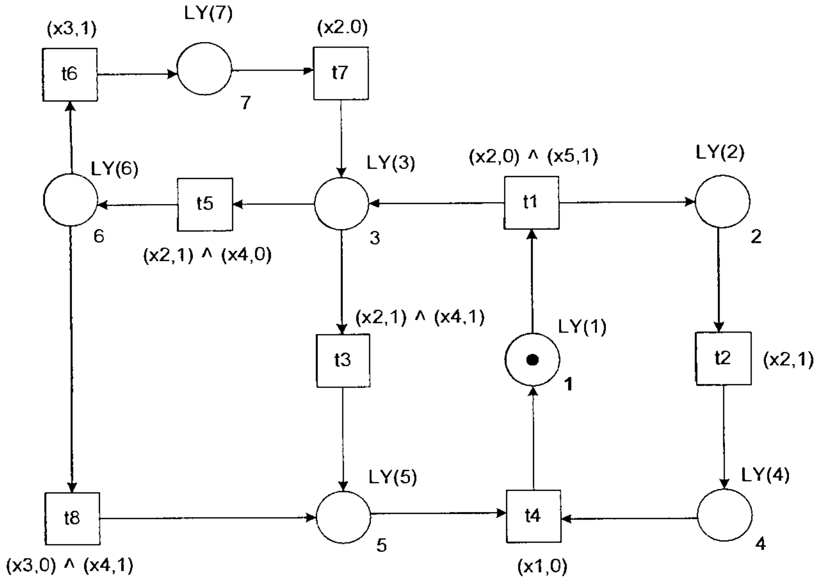

LY(1) = {(u1,0),(u2,0),(u3,0),(u4,0),(u5,0)},
LY(2) = {(u5,0)},
LY(3) = {(u1,1),(u2,0),(u3,0),(u4,0)},
LY(4) = {(u5,1)},
LY(5) = {(u1,0),(u2,0),(u3,1),(u4,0)},
LY(6) = {(u1,0),(u2,1),(u3,0),(u4,0)},
LY(7) = {(u1,0),(u2,0),(u3,0),(u4,1)}

Fig. 2. Graphical representation of I-P/T-system

Theorem 2. [13] For every B-system BS = (P, T, F, δ, m_0, η) the following propositions are true:

(1) $|\eta| = \frac{1}{2}|P|$, (2) $\forall(p_j^0, p_j^1) \in \eta: \{p_j^0, p_j^1\}$ is a P-invariant, (3) $\forall(p_j^0, p_j^1) \in \eta: p_j^{0\bullet} \cap {}^{\bullet}p_j^1 \neq \emptyset \vee p_j^{1\bullet} \cap {}^{\bullet}p_j \neq \emptyset$, (4) $\forall t \in T: |{}^{\bullet}t| = |t^{\bullet}|$, (5) PS is a 1-P/T-system.

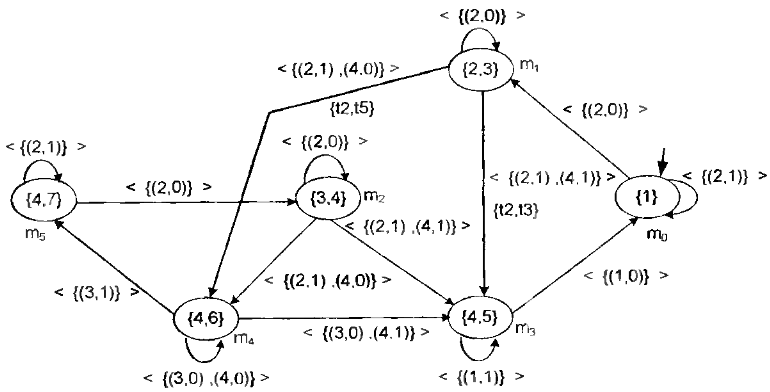

Outputs

$\Lambda(m_0) = \{(1,0),(2,0),(3,0),(4,0),(5,0)\}$, $\Lambda(m_1) = \{(1,1),(2,0),(3,0),(4,0),(5,0)\}$,
$\Lambda(m_2) = \{(1,1),(2,0),(3,0),(4,0),(5,1)\}$, $\Lambda(m_3) = \{(1,0),(2,0),(3,1),(4,0),(5,1)\}$,
$\Lambda(m_4) = \{(1,0),(2,1),(3,0),(4,0),(5,1)\}$, $\Lambda(m_5) = \{(1,0),(2,0),(3,0),(4,1),(5,1)\}$

Fig. 3. Diagram of Moore automaton generated by 1-P/T-system specified in Fig. 2

3. PLC LADDER DIAGRAM LANGUAGE

Ladder diagrams are an industrial programming language typically used on programmable logic controllers (PLC). The ladder diagram (LD), as a PLC language, consists of two vertical lines representing the power rails. Rungs of LD are circuits connected as horizontal lines between the power rails. The left part of the rang consists of symbols depicted by double vertical lines (resp. slashed), they are units which are characterized by the property that they turn conductible if the corresponding inputs are true (resp. false). The ellipse (or ellipses) placed on the right part of the rung represents the output. Each rung on the LD defines one operation in the control process.

The LD shown in Fig. 4 describes the control process of the neutralization tank system presented in Example 1. The p-th rung from the top of LD is denoted by lp. In this paper, it is assumed that the type of inputs and outputs is restricted to binary variables. For an LD consisting of n rungs, each output is calculated in PLC by scanning from the first rung to the n-th rung. The controlled plant is driven according to the output signals obtained immediately after each scanning. The scanning process is presented in Fig. 5.

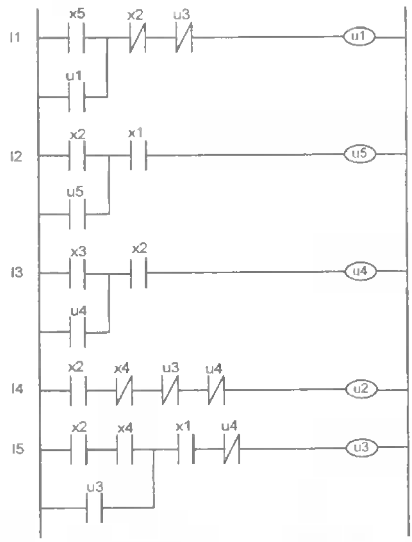

Fig. 4. [12] Ladder diagram for the neutralization tank system control process. The plant is shown in Fig. 6

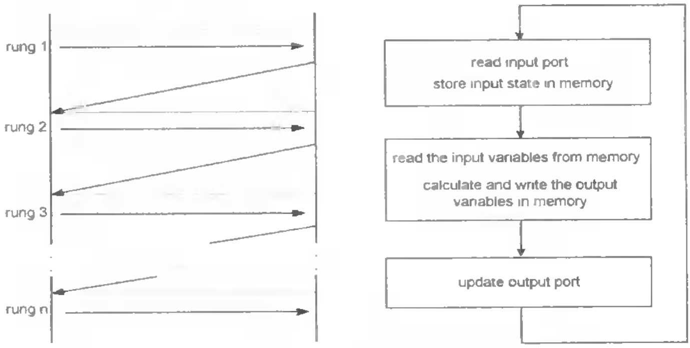

Fig. 5. Scanning process of the LD program

Example 1. Neutralization tank system [12]
The specification for the plant shown in Fig. 6 is given as follows:

1. At the initial state, all of the valves and the mixer should be off and the tank is empty.
2. When the starting switch turns on, open valve U1.
   Inject liquid from reservoir unless x2 = 1.
   2.a. Keep injecting liquid from reservoir. The mixer starts when x2 = 1.
   2.b. Sensor x4 detects pH of liquid. If the value does not reach the specified pH value, then open valve U2 to inject a neutralizing agent.
3. Keep injecting the neutralizing agent. If sensor x3 = 1, stop injecting the neutralizing agent and open valve U4 to drain the liquid until the liquid level is at the position of sensor x2. Close valve U4 again and go back to the process 2.b.
4. If pH of the liquid is satisfied (process completed), close valve U2 and drain the mixed liquid through valve U3. After that, if x1 turns to 0 due to decrease of the liquid level, close valve U3 and go to the process 1.

The LD satisfying the above specification is shown in Fig. 4.

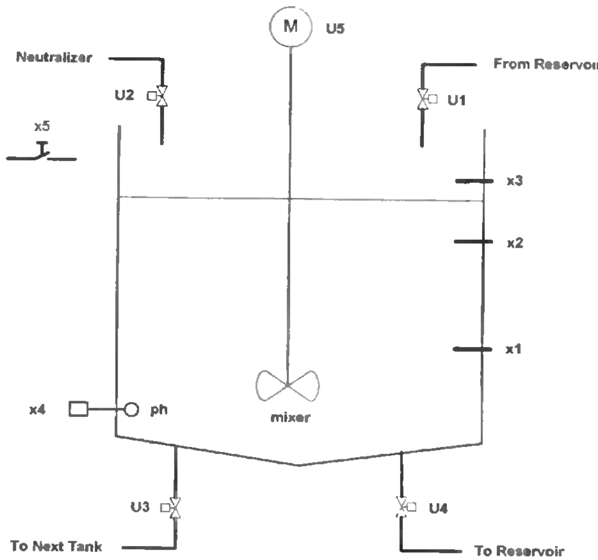

Fig. 6. Neutralization tank system

4. MODLING OF THE PLC LADDER DIAGRAMS

The defined below LD-P/T-system is based on the B-system from definition 8. It is a model of the behavior of PLC which was programmed in LD language. LD scanning was carried out with the help of the function ordscan. The subset of places named Pout represents these LD elements, whose state is being copied to the state of the PLC output port. The model can be enriched with additional elements for example timers, but this aspect has been omitted due to space limits.

Definition 8. LD- P/T-system is every eight-tuple LDPS = (BS, ordscan, XB,YB, LX, LY, $\delta^{\sim}$, Λ), in which BS = (P, T, F, δ, m_0,η) is a B-system, where: P = Pout ∪ Pint, and Pint = P \ Pout, Pout is an output places set,
ordscan: $\{1,2,\ldots,|T|\} \rightarrow T$ is a bijection, which orderings transitions with respect LD scanning order, XB, YB, LX, EVAL are described in def. 6,
LY: Pout → $\{a \subseteq Y\times\{0,1\} \mid \exists u\in YB: a \subseteq \bar{\bar{u}}\}$ is a Pout labeling function, which value is computed under formula: $\forall m \in M, \exists u\in YB: \bigcup_{p\in]m[_{Pout}} LY(p) \subseteq \bar{\bar{u}}$, where M is a set of reachable markings of BS, $\bar{\bar{u}} = \{(y, i) \in Y\times\{0, 1\} \mid i = u(y)\}$.
$\delta^{\sim}$: M × XB → M is an external transition function of LDPS, which is computed according to formula: $\forall(m, w) \in M \times XB: \delta^{\sim}(m, w) = \delta_{|T|,w}\left(\delta_{|T|-1,w}\left(\ldots\, \delta_{2,w}\left(\delta_{1,w}(m)\right)\right)\right)$,

$$\delta_{i,w}: M \rightarrow M,\ \delta_{i,w}(m) = \begin{cases} m, & ordscan(i) \notin sel(m, w) \\ \delta(m, ordscan(i)), & ordscan(i) \in sel(m, w) \end{cases},$$

$sel(m, w) = SEL(w) \cap m^{\bullet\bullet}$, SEL: XB → 2^T,
where $SEL(w) = \{t\in T \mid EVAL(w, LX(t)) = True\}$.
Λ: M → YB^{-} is an output function of LDPS. Value of the function is computed according to formula: $\forall m\in M, \forall y\in Y: \Lambda(m) = \bigcup_{p\in]m[_{Pout}} LY(p)$.

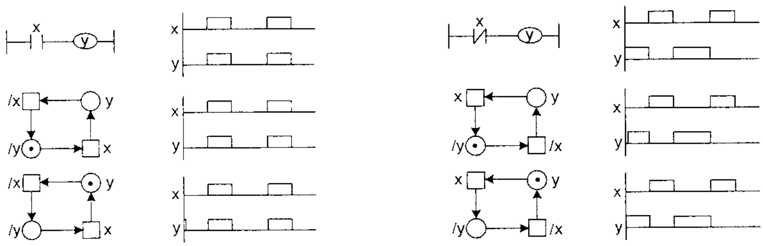

Fig. 7. Modeling semantic

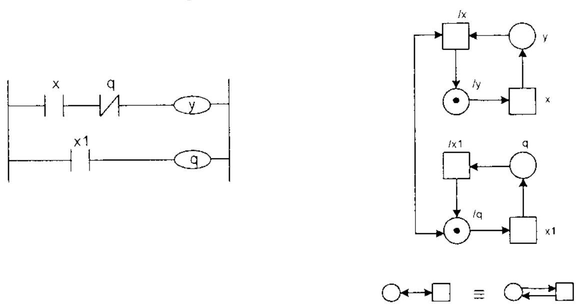

Fig. 8. LD inner feedback modeling example

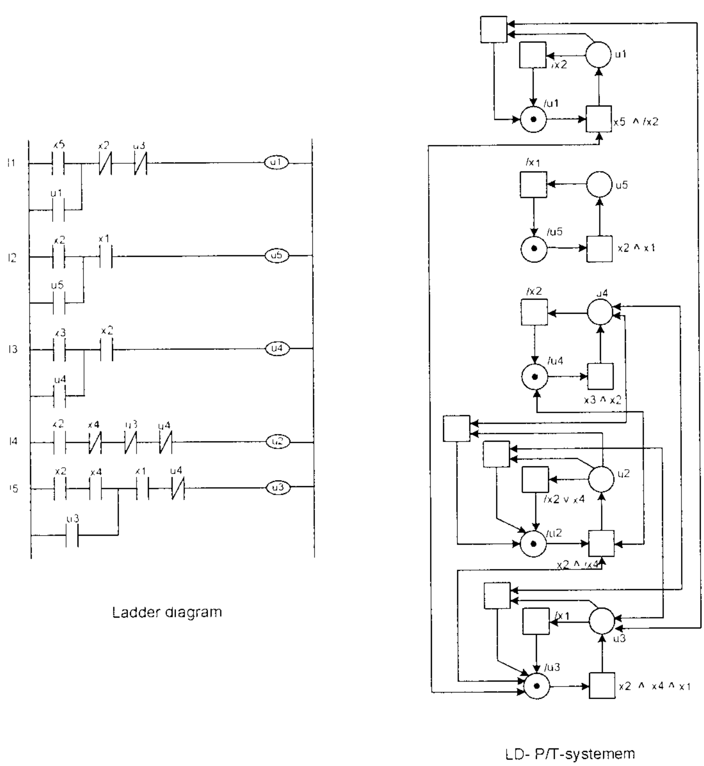

Fig. 9. Ladder diagram for the neutralization tank system from example 1 and its LD-P/T-system graphical model

Algorithm for generating global states transitions diagram of closed loop system consists of LD-P/T-system and the plant is presented in appendix B. State-transition diagram, as result of the algorithm, is presented in Fig. 12. Examined Example 1 was taken from [12]. The proposed there method of the generation state-transition diagram for closed loop system for controller-plant is based on the theory of difference equation. Our result for the same example differs in the fact, that transition ((1,1, 0,0), (0,1,0,0,1)) → ((1,1,0,1), (0,0,1,0,1)) from diagram presented in Fig. 12, is missing in [12]. The LD is simple, so it is easy to prove that the transition exists.

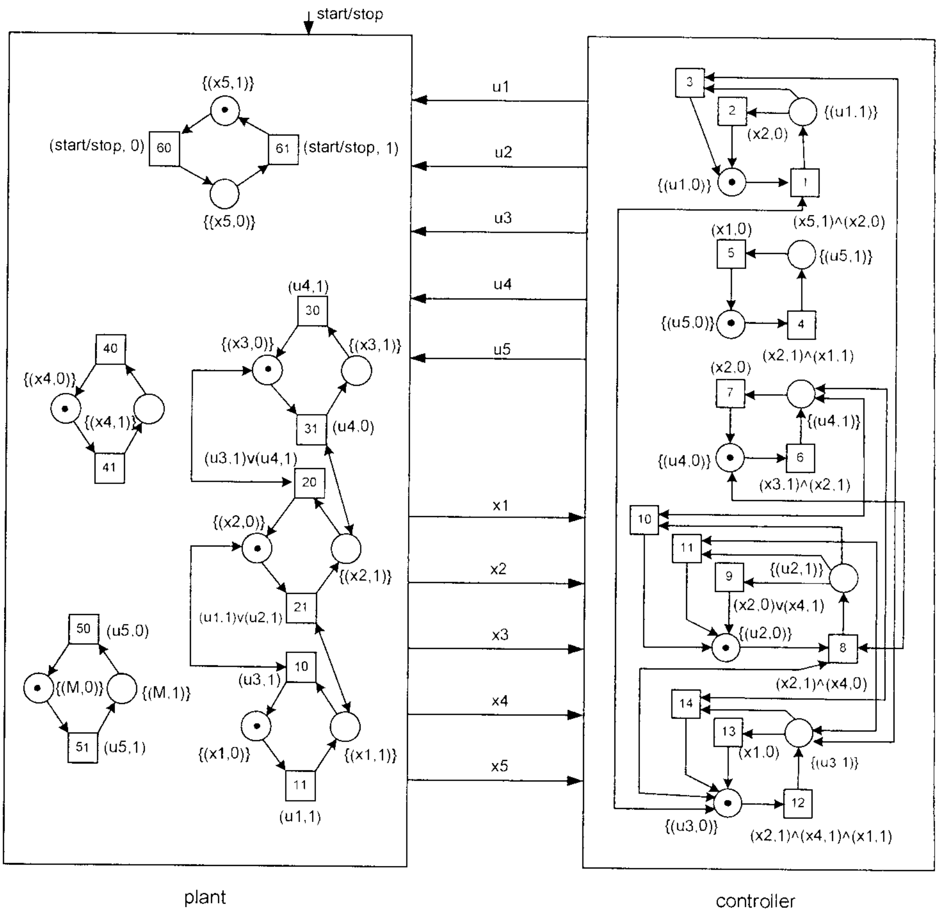

Fig. 10. Closed loop system controller-plant for example 1

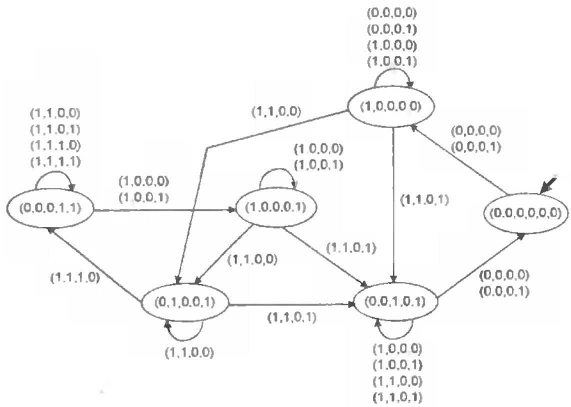

Fig. 11. Diagram of Moore automaton generated by LD-P/T-system of controller

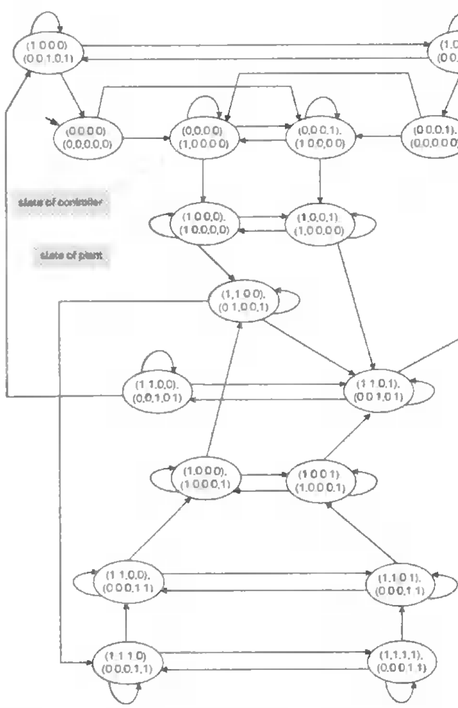

Fig. 12. Global states transitions diagram for closed loop system controller-plant from Fig. 10

The diagram shown in Fig. 11 represents Moore automaton generated by LD-P/T-controller system. It is simple to calculate – in frames of the same model – the automaton by supplementing a little the existing algorithm. This Moore automaton constitutes the base for the new I-P/N-system synthesis. The new system more precisely describes the behavior of controller, since it presents the information about the sequence of events in an open way. The I-P/N-system, for example 1, is presented in fig. 2. The behavior of this system is isomorphic to the behavior of LD-P/T-system presented in

Fig. 11. Description of the control algorithm in the form of I-P/N-system gives the possibility of its implementation via technology different than PLC technology, for example FPGA. [1, 13] It can be important when we deal with the embedded system.

5. CONCLUSION

In this paper, several models based on Petri nets have been considered. We propose a new model of PLC ladder diagram and algorithm to compute the state space of the closed loop system which consists of a controller and a plant. This result has a potential of being applied for fault handling and synthesis of new models of controllers which can be carried out on FPGA platforms[1, 13, 4]. Future subjects include LD-VHDL transformation for FPGA implementation.

APPENDIX

A. I-P/T-system

Specification of I-P/T-system from fig. 2:

```
PN={'t1':[{1},{2,3}],'t2':[{2},{4}],'t3':[{3},{5}],'t4':[{4,5},{1}],'t5':[{3},{6}],'
t6':[{6},{7}],
't7':[{7},{3}],'t8':[{6},{5}]}
P={1,2,3,4,5,6,7}
m=frozenset({1})
LX={'t1':(2,0),'t2':(2,1),'t3':((2,1),(4,1),'and'),'t4':(1,0),'t5':((2,1),(4,1),'and
'),'t6':(3,1),'t7':(2,0),'t8':((3,0),(4,1),'and')}
LY={ 1:{(1,0),(2,0),(3,0),(4,0),(5,0)}, 2: {(5,0),(4,1)},
3:{(1,1),(2,0),(3,0),(4,0)}, 4: {(5,1)}, 5:{(1,0),(2,0),(3,1),(4,0)}, 6:
{(1,0),(2,1),(3,0),(4,0)}, 7: {(1,0),(2,0),(3,0),(4,1)} }
XB={0: (0, 1, 0, 0), 1: (0, 1, 1, 0), 2: (0, 0, 1, 0), 3: (0, 0, 1, 1), 4: (0, 1, 1,
1), 5: (0, 1, 0, 1), 6: (0, 0, 0, 1), 7: (1, 0, 1, 1), 8: (1, 0, 0, 1), 9: (1, 1, 0,
1), 10: (1, 1, 0, 0), 11: (1, 0, 0, 0), 12: (1, 0, 1, 0), 13: (1, 1, 1, 0), 14: (0,
0, 0, 0), 15: (1, 1, 1, 1)}
X={1,2,3,4}
Y={1,2,3,4,5,6}
```

(modules are coded with using Python 3)

Module for EVAL: XB × FB(X × {0,1}) → {True, False}

```
LX={'t1':(2,0),'t2':(2,1),'t3':(((2,1),(4,0),'and'),((3,1),(1,1),'and'),'or'),'t4':(
1,0),'t5':((2,1),(4,0),'and'),'t6':(3,1),'t7':(2,0),'t8':((3,0),(4,1),'and')}
XB={0:(0, 0, 0, 1),1: (1, 0, 0, 1), 2: (1, 1, 0, 1), 3: (1, 1, 0, 0), 4: (1, 0, 0,
0), 5: (1, 1, 1, 0), 6: (0, 0, 0, 0), 7: (1, 1, 1, 1)}
tranz='t3', number_w=2
fb =LX[tranz]= (((2,1),(4,0),'and'),((3,1),(1,1),'and'),'or')
w = XB[2]= (1, 1, 0, 1) # Remark 2
input: (1, 1, 0, 1), (((2,1),(4,0),'and'),((3,1),(1,1),'and'),'or')
output: False
def ev(w,fb1):
 if fb1==True:
 return True
 elif fb1==False:
 return False
 return fb1[1]==XB[w][fb1[0]-1]

def EV(fb2):
 if fb2[2]=='and':
 val=fb2[0] and fb2[1]
 elif fb2[2]=='or':
 val=fb2[0] or fb2[1]
 return val
def EVAL(w,fb):
```

```
if fb==():
return True
elif fb!=() and len(fb)<=2:
return ev(w,fb)
elif len(fb)>2:
temp1=EVAL(w,fb[0])
temp2=EVAL(w,fb[1])
temp3=(temp1,temp2,fb[2])
return EV(temp3)
```

Module for sel: $M \times XB \rightarrow 2^T$

```
def fo(mark):
 return {t for t in sorted(PN) if PN[t][0] <= mark}

def SEL(w):
 return {i for i in sorted(LX) if EVAL(w,LX[i])==True}

def sel(mark,w):
 return SELw(w)&fo(mark)
```

 # fo(mark) = mark••

Module for stepTest: $2^{sel(m,w)} \rightarrow \{True, False\}$

```
def stepTest(TrSet):
 preTrSet=set()
 postTrSet=set()
 log=True
 temp=tuple(TrSet)
 temp1=list(temp)
 for i in range(len(temp)):
 preTrSet.update(PN[temp[i]][0])
 postTrSet.update(PN[temp[i]][1])
 temp1.remove(temp[i])
 for j in temp1:
 b=PN[temp[i]][0]&PN[j][0]==set()
 c=log and b
 log=c
 temp1=list(temp)
 return [log,preTrSet,postTrSet]
```

#stepTest(TrSet)[0] = log = stepTest(TrSet),
#PreTrSet = pre(TrSet) = $\cup_{t\in TrSet} {}^{\bullet}t$, PostTrSet = post(TrSet) = $\cup_{t\in TrSet} t^{\bullet}$

Module for ∂' : $M \times XB \rightarrow M \cup \{('NONDETERMINISM for', arg1, arg2)\}$

```
def ExtTrans(mark,w):
 TrSet=sel(mark,w)
 if TrSet==set():
 return mark
 elif TrSet!=set() and stepTest(TrSet)[0]:
 return (mark - stepTest(TrSet)[1]) | stepTest(TrSet)[2]
 elif not stepTest(TrSet)[0]:
 print('NONDETERMINISM for', mark, TrSet)
 return mark
```

Module for Λ: $M \rightarrow YB^{-}$

```
def lamb(mark):
 out_mark1=set()
 for p in mark:
 out_mark1.update(LY[p])
 return out_mark1
def LAMBDA(mark):
 out_mark=lamb(mark)
 temp={i[0] for i in out_mark}
 temp3=frozenset(Y)
 temp1=Y
 temp1.difference_update(temp)
 temp2={(j,'-') for j in temp1}
 out_mark.update(temp2)
 test={i for i in temp3 if ({(i,0),(i,1)} <= out_mark)}
```

```
 if test != set():
 print('LY incorrect for', test, mark)
 return out_mark
```

Module for A(IPS) generating (breadth_first_search method)[2]

```
From=RM={m}
Arcs={}
def XBnextM(From1,NM1,Arcs1):
 for curr_mark in From1:
 for i in sorted(XB):
 next_mark=ExtTrans(curr_mark,i)
 NM1.update({next_mark})
 aa=(curr_mark,next_mark)
 bb=XB[i]
 if aa in Arcs1.keys():
 Arcs1[aa].append(bb)
 else:
 Arcs1.update({aa:[bb]})
 return [NM1, Arcs1]
def XBreachM(From):
 NM=set()
 while len(From) > 0:
 From = XBnextM(From,NM,Arcs)[0].difference(RM)
 RM.update(From)
 return Arcs,RM
OutputMap={i:LAMBDA(i) for i in XBreachM(From)[1]}
print('Arcs =',XBreachM(From)[0])
print('Outputs =',OutputMap)
Arcs = {(frozenset({2, 3}), frozenset({4, 5})): [(0, 1, 1, 1), (0, 1, 0, 1), (1, 1,
0, 1), (1, 1, 1, 1), (0, 1, 1, 1), (0, 1, 0, 1), (1, 1, 0, 1), (1, 1, 1, 1)],
(frozenset({2, 3}), frozenset({2, 3})): [(0, 0, 1, 0), (0, 0, 1, 1), (0, 0, 0, 1),
(1, 0, 1, 1), (1, 0, 0, 1), (1, 0, 0, 0), (1, 0, 1, 0), (0, 0, 0, 0), (0, 0, 1, 0),
(0, 0, 1, 1), (0, 0, 0, 1), (1, 0, 1, 1), (1, 0, 0, 1), (1, 0, 0, 0), (1, 0, 1, 0),
(0, 0, 0, 0)], ..........................
.............................................................................................
Outputs = {frozenset({3, 4}): {(3, 0), (2, 0), (5, 1), (1, 1), (4, 0)},
frozenset({2, 3}): {(2, 0), (5, 0), (3, 0), (4. 1), (1, 1), (4, 0)}, frozenset({4,
6}): {(3, 0), (5, 1), (1, 0), (2, 1), (4, 0)}, frozenset({4, 7}): {(3, 0), (5, 1),
(1, 0), (4, 1), (2, 0)}, frozenset({1}): {(3, 0), (2, 0), (1, 0), (5, 0), (4, 0)},
frozenset({4, 5}): {(4, 0), (5, 1), (1, 0), (3, 1), (2, 0)}}
```

B. Listing for global states transitions diagram of closed loop system consists of LD-P/T-system and plant

(with using Python 3)

Specification of LD-P/T-system (controller) from fig. 10:

```
PNLD={1:[{(1,0),(3,0)},{(1,1),(3,0)}],2:[{(1,1)},{(1,0)}],3:[{(1,1),(3,1)},{(1,0),(3
,1)}],4:[{(5,0)},{(5,1)}],5:[{(5,1)},{(5,0)}],6:[{(4,0)},{(4,1)}],7:[{(4,1)},{(4,0)}
],8:[{(2,0),(4,0),(3,0)},{(2,1),(4,0),(3,0)}],9:[{(2,1)},{(2,0)}],10:[{(2,1),(4,1)},
{(2,0),(4,1)}],11:[{(2,1),(3,1)},{(2,0),(3,1)}],12:[{(3,0),(4,0)},{(3,1),(4,0)}],13:
[{(3,1)},{(3,0)}],14:[{(3,1),(4,1)},{(3,0),(4,1)}]}
Pl={(1,1),(1,0),(5,1),(5,0),(4,1),(4,0),(2,1),(2,0),(3,1),(3,0)}
ml=frozenset({(1,0),(5,0),(4,0),(2,0),(3,0)})
LXl={1:(2,0),2:(2,1),3:(),4:((1,1),(2,1),'and'),5:(1,0),6:((3,1),(2,1),'and'),7:(2,0
),8:((2,1),(4,0),'and'),9:((2,0),(4,1),'or'),10:(),11:(),12:(((2,1),(4,1),'and'),(1,
1),'and'),13:(1,0),14:()}
LYl={'11':{(1,1)},'10':set(),'51':{(5,1)},'50':set(),'41':{(4,1)},'40':set(),'21':{(
2,1)},'20':set(),'31':{(3,1)},'30':set()}
XBl={0:(0, 0, 0, 1),1: (1, 0, 0, 1), 2: (1, 1, 0, 1), 3: (1, 1, 0, 0), 4: (1, 0, 0,
0), 5: (1, 1, 1, 0), 6: (0, 0, 0, 0), 7: (1, 1, 1, 1)}
```

Specification of I-P/T-system (plant) from fig. 10:

```
PNPL={'11':[{(1,0)},{(1,1)}],'10':[{(1,1),(2,0)},{(1,0),(2,0)}],'21':[{(2,0),(1,1)},
{(2,1),(1,1)}],'20':[{(2,1),(3,0)},{(2,0),(3,0)}],'31':[{(3,0),(2,1)},{(3,1),(2,1)}]
,'30':[{(3,1)},{(3,0)}],'41':[{(4,0)},{(4,1)}],'40':[{(4,1)},{(4,0)}]}
Pp={(1,1),(1,0),(2,1),(2,0),(3,1),(3,0),(4,1),(4,0)}
```

---

[2] Idea of the method was adopted from [3], which was used in generating reachable markings of Petri nets

```
mp=frozenset({(1,0),(2,0),(3,0),(4,0)})
LXp={'11':(1,1),'10':(3,1),'21':((1,1),(2,1),'or'),'20':((3,1),(4,1),'or'),'31':(2,1
),'30':(4,1),'41':(),'40':()}
XBp={0: (0, 1, 0, 0), 1: (0, 1, 1, 0), 2: (0, 0, 1, 0), 3: (0, 0, 1, 1), 4: (0, 1,
1, 1), 5: (0, 1, 0, 1), 6: (0, 0, 0, 1), 7: (1, 0, 1, 1), 8: (1, 0, 0, 1), 9: (1, 1,
0, 1), 10: (1, 1, 0, 0), 11: (1, 0, 0, 0), 12: (1, 0, 1, 0), 13: (1, 1, 1, 0), 14:
(0, 0, 0, 0), 15: (1, 1, 1, 1)}
```

Signal x5 is switched on (x5, 1) and omitted, since it is the one which is accepted only in the initial state. For this reason transitions '60','61' are not presented in the specification. Transitions '50' and '51' are omitted also because the mixer does not exert a direct influence on the state of the controller.

```
def nextLDstate(NLD,s,LX1):
 #fitting marking of the LD-controller to state s[1]
 mark1={(i+1,s[1][i]) for i in range(len(s[1]))}
 #-----------------------------------------------
 #LD-controller marking and output state updating according to
 #sequence of rungs
 TrList=sorted(LX1)
 tt=TrList[0]
 z=mark1
 while tt <= TrList[len(TrList)-1]:
 if tt in sel(z,s[0],NLD,LX1):
 nn = (z - NLD[tt][0]) | NLD[tt][1]
 z=nn
 else:
 nn=z
 tt1=tt+1
 tt=tt1
 mn1=nn
 #---------------------------------------------
 #fitting output of the LD-controller to new marking
 mn1list=list(mn1)
 OutLDdic={i[0]:i[1] for i in mn1list}
 OutLD=[OutLDdic[i] for i in sorted(OutLDdic)]
 OutLD1=tuple(OutLD)
 #---------------------------------------------
 #global state updating
 s1=(s[0],OutLD1)
 return s1

def nextPL_LDstate(NLD,NPL,s,NewStates1,transArc1):
 #LD-controller reaction, storage of new global state and transition arc
 z0=nextLDstate(NLD,s,LX1)
 NN1.update({z0})
 transArc1.update({(s,z0)})
 #------------------------
 #fitting marking of the plant to state s[0]
 markp={(i+1,s[0][i]) for i in range(len(s[0]))}
 TrSetp=sel(markp,s[1],NPL,LXp)
 for t in TrSetp:
 #next marking of plant
 #no steps, since the reaction of the plant is slower than the controller reaction
 new_markp=(markp - NPL[t][0]) | NPL[t][1]
 #fitting output of the plant to new marking
 new_mark1List=list(new_markp)
 new_mark1List.sort()
 OutPLdic={i[0]:i[1] for i in new_mark1List}
 OutPL=[OutPLdic[i] for i in sorted(OutPLdic)]
 OutPL1=tuple(OutPL)
 #global state updating
 z2=(OutPL1,s[1])
 #---------------------------
 #---------------------------------------------
 #LD controller reaction, storage of new global state and transition arc
 #(for every new state of output of the plant)
 z3=nextLDstate(NLD,z2,LX1)
 NewStates1.update({z3})
 transArc1.update({(s,z3)})
```

```
 return NewStates1,transArc1

From=ReachStates={s0}
transArc2=set()
def Simage(NLD,NPL,From):
 NewStates=set()
 transArc=set()
 for state in From:
 nextPL_LDstate(NLD,NPL,state,NewStates,transArc)
 return NewStates,transArc

def ReachS(NLD,NPL,From):
 while From!=set():
 temp=Simage(NLD,NPL,From)[1]
 transArc2.update(temp)
 From=Simage(NLD,NPL,From)[0].difference(ReachStates)
 ReachStates.update(From)
 return ReachStates,transArc2

print(ReachS(PNLD,PNPL,From)[1])

{(((1, 0, 0, 1), (1, 0, 0, 0, 1)), ((1, 0, 0, 0), (1, 0, 0, 0, 1))), (((1, 0, 0, 1),
(0, 0, 1, 0, 1)), ((0, 0, 0, 1), (0, 0, 0, 0, 0))), (((1, 1, 1, 1), (0, 0, 0, 1,
1)), ((1, 1, 1, 1), (0, 0, 0, 1, 1))), (((1, 1, 1, 1), (0, 0, 0, 1, 1)), ((1, 1, 1,
0), (0, 0, 0, 1, 1))),.............................................................
...................................................................................
```

BIBLIOGRAPHY

[1] Adamski M., Monteiro J. L., 2000. From Interpreted Petri Net Specification to Reprogrammable Logic Controllers, Indusrial Electroncs, ISIE'2000. Proceedings of the 2000. Cholula, Pueblo: IEEE, 2000. 13-19.

[2] Bernardinello L., Ferigato C., Pomello L., 2003. An Algebraic model of observable properties in distributed systems, TCS.

[3] Cortadella J., Kishnievsky M., Lavagno L., Yakovlev A., 1998. Derevating Petri Nets From Finite Transitin Systems, IEEE Trans on Comp. Vol. 47, No. 8.

[4] Du D., Liu Y., Guo X., Yamazaki K., 2008. Study on LD-VHDL conversion for FPGA-based PLC implementation, Int. J. Adv. Manuf. Technol. Springer-Verlag.

[5] Fujimoto, Y., 2002. Design of Discrete time Polinominal Nonlinear Systems and Its Application to Sequential Control, T. IEE Japan, Vol 122-D, No. 9, 918-927.

[6] Girauld C., Valk R., 2001. Petri Nets for System Engineering, Berin, Springer-Verlag.

[7] Lee, Jin-Shyan, Chun-Chieh Chuang, 2009. Development of a Petri net-based fault diagnostic system for industrial processes, Industrial Electronics, IECON '09. 35th Annual Conference of IEEE, 4347-4352.

[8] Nielsen M., Rozenberg G., Thiagarajan P.S., 1992. Elementary Transition Systems, TCS 96.

[9] Pastor E., Cortadella J., Roig O., 2001. Symbolic Analysis of Bounded Petri Nets, IEEE Tras. on Comp. Vol. 50, No. 5.

[10] Reisig, W., 1988. Sieci Petiego. WNT Warszawa.

[11] Wright D., (Chair)., 2004. IEEE Standards for VHDL Register Transfer Level (RTL) Synthesis. IEEE Std 1076.6- 2004, New York, IEEE.

[12] Zanma T., Miyabayashi T., Ishida M., 2004. Sequence generation of discrete event system and logic controller and its applicability to fault detection, Advanced Motion Control, AMC '04. The 8th IEEE International Workshop on Digital Object Identifi,: 10.1109/AMC.2004.1297936, 601-606.

[13] Zech W., 2008. Właściwości struktury sieci Petriego i ich wykorzystanie do syntezy układów sterownia binarnego, rozprawa doktorska. Politechnika Poznańska.

MODELE SYSTEMÓW ZDARZEŃ DYSKRETNYCH SKONSTRUOWANE W OPARCIU O SIECI PETRIEGO I GENERACJA SEKWENCJI STANÓW ZAMKNIĘTEGO SYSTEMU OBIEKT-STEROWNIK

Streszczenie

W artykule przedstawiono formalny model diagramu drabinkowego (LD) jako LD-P/T-system. Skonstruowano model zamkniętej pętli sprzężenia między sterownikiem (LD) i sterowanym obiektem. Przedstawiono algorytm generacji diagramu przejść między stanami takiego systemu. Możliwa jest detekcja uszkodzenia, gdy wygenerowany zostanie nieprzewidziany stan. Dodatkowa korzyść z takiego podejścia wynika z faktu, że możliwa jest konstrukcje diagramu przejść samego sterownika, co może być wykorzystane do transformacji diagramów drabinkowych na model dający się opisać w języku VHDL i implementować w FPGA.

Słowa kluczowe: system zdarzeń dyskretnych, sieci Petriego, programowalne sterowniki sekwencyjne, diagramy drabinkowe

UNIWERSYTET TECHNOLOGICZNO-PRZYRODNICZY
IM. JANA I JĘDRZEJA ŚNIADECKICH W BYDGOSZCZY
ZESZYTY NAUKOWE NR 260
TELEKOMUNKACJA I ELEKTRONIKA 15 (2011), 37-48

NETWORK ANOMALY DETECTION BASED ON ADAPTIVE APPROXIMATION OF SIGNALS

Łukasz Saganowski, Tomasz Andrysiak

Institute of Telecommunications,
Faculty of Telecommunications and Electrical Engineering
University of Technology and Life Sciences (UTP)
ul. Kaliskiego 7, 85-789 Bydgoszcz, Poland
[luksag, andrys]@utp.edu.pl

Summary: In the article we present Anomaly Detection System for recognizing unknown threats in network traffic with the use of Matching Pursuit decomposition. We proposed further improvements of presented anomaly detection method. Efficiency of our method is reported with the use of extended set of benchmark test traces. At the end we compared achieved results with different methods based on signal processing, data mining and hybrid techniques.

Keywords: Anomaly Detection System, Matching Pursuit decomposition, Adaptive approximation of signals

1. INTRODUCTION

Anomaly detection approach is a new, emerging trend for network security especially for high-security networks (such as military or critical infrastructure monitoring networks). Such networks are currently exposed to many threats due to the fact that barriers between trusted and un-trusted network components do not successfully protect critical parts of the cyber domain. Most IDS/IPS (Intrusion Detection/Prevention Systems) cannot cope with new sophisticated malware (viruses, SQL injections, Trojans, spyware and backdoors) and 0-day attacks. Most current IDS/IPS systems have problems in recognizing new attacks (0-day exploits) since they are based on the signature-based approach. In such mode, when system does not have an attack signature in database, the attack is not detected. Another drawback of current IDS systems is that the used parameters and features do not contain all the necessary information about traffic and events in the network [1].

Intrusion Detection Systems (IDS) can be classified as belonging to two main groups depending on the detection technique employed:

- signature-based detection,
- anomaly detection.

Anomaly Detection techniques rely on the existence of a reliable characterization of what is normal and what is not, in a particular networking scenario. More precisely, Anomaly Detection techniques base their evaluations on a model of what is normal, and classify as anomalous all the events that fall outside such a model. In this paper, a new solution for Anomaly Detection System (ADS) – system based on signal processing algorithm - is presented. ADS analyzes traffic from internet connection in certain point of a computer network. The proposed ADS system uses redundant signal decomposition method based on Matching Pursuit algorithm.

Our original methodology [29] for network security anomaly detection based on Matching Pursuit is presented and evaluated using network data traces from different sources [20, 21, 22]. We also compared Matching Pursuit approach to different methods based on signal processing (e.g. Discrete Wavelet Transform) and statistical analysis.

2. SIGNAL PROCESSING METHODS FOR NETWORK ANOMALY DETECTION

Signal processing techniques have found application in Network Intrusion Detection Systems because of their ability to detect novel intrusions and attacks, which cannot be achieved by signature-based approaches. It has been shown that network traffic presents several relevant statistical properties when analyzed at different levels (e.g. self-similarity, long range dependence, entropy variations, etc.) [4]. Approaches based on signal processing and on statistical analysis can be powerful in decomposing the signals related to network traffic, giving the ability to distinguish between trends, noise, and actual anomalous events. Wavelet-based approaches, maximum entropy estimation, principal component analysis techniques, and spectral analysis, are examples in this regard which have been investigated in the recent years by the research community [5-9]. A powerful analysis, synthesis, and detection tool in this field is represented by the wavelets. Indeed, time and scale-localization abilities of the wavelet transform, make it ideally suited to detect irregular traffic patterns in traffic traces. Recently many wavelet-based methods for detection of attacks have been tested and documented. Some are based on the continuous wavelet transform analysis, most of them however refer to the Discrete Wavelet transformation and the multiresolution analysis [4].

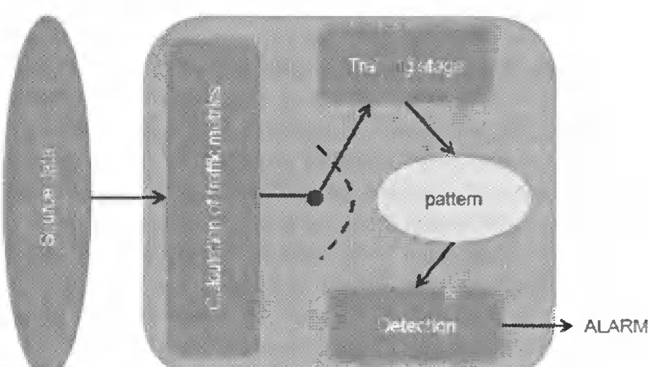

Fig. 1. Basic conception of Anomaly Detection System for network traffic [30].

However, Discrete Wavelet Transform provides a large amount of coefficients which not necessarily reflect required features of the network signals. Therefore, in this paper we propose another signal processing and decomposition method for anomaly/intrusion detection in networked systems. We developed original Anomaly Detection ADS algorithm based on Matching Pursuit [29]. The general overview of our Anomaly Detection System is presented in Figure 1.

3. ADAPTIVE APPROXIMATION OF SIGNAL FOR ANOMALY DETECTION

Given an overcomplete set of functions called dictionary $D = \{g_{\gamma_0}, g_{\gamma_1}, \dots, g_{\gamma_{n-1}}\}$ such that norm $\|g_{\gamma_i}\| = 1$, we can define an optimal M – approximation as an expansion, minimizing the error δ of an approximation of signal $f(t)$ by M waveforms g_{γ_i} called atoms:

$$\delta = \left\|f(t) - \sum_{i=0}^{M-1} \alpha_i g_{\gamma_i}\right\|, \tag{1}$$

where functions $g_{\gamma_i} \in L^2(R)$ and $\{\gamma_i\}_{i=1,2..,M}$ represents the indices of the chosen functions g_{γ_i} [12]. Finding such an optimal approximation is an NP-hard problem [13]. A suboptimal expansion can be found by means of an iterative procedure, such as the matching pursuit algorithm.

3.1. Matching pursuit overview

Matching pursuit is a recursive, adaptive algorithm for signal decomposition [11]. The matching pursuit decomposes any signal into linear expansion of waveforms witch are taken from an overcomplete dictionary D. Signal f can be written as the weighted sum of dictionary elements:

$$f = \sum_{i=0}^{N-1} \alpha_i g_{\gamma_i} + R^n f, \tag{2}$$

where $R^n f$ is residual in an n – term sum.

In the first step of Matching Pursuit algorithm, the waveform g_{γ_0} which best matches the signal f is chosen. The first residual is equal to the entire signal $R^0 = f$. In each of the consecutive steps, the waveform g_{γ_n} is matched to the signal $R^n f$, which is the residual left after subtracting results of previous iterations:

$$R^n f = R^{n-1} f - \alpha_n g_{\gamma_n}, \tag{3}$$

where

$$\alpha_n = \langle R^{n-1} f, g_{\gamma_n} \rangle \tag{4}$$

and

$$g_{\gamma_n} = arg\max_{g_{\gamma_i} \epsilon D} \left|\langle R^{n-1} f, g_{\gamma_i} \rangle\right|. \tag{5}$$

When $R^n f$ is minimized for a given $g_{\gamma_{n-1}}$, the projection between the previous residue and actual atom $\langle R^{n-1} f, g_{\gamma_{n-1}} \rangle$ is maximized. Iteratively, we obtain for N atom:

$$R^N f = f - \sum_{n=0}^{N-1} \langle R^n f, g_{\gamma_n} \rangle g_{\gamma_n}, \tag{6}$$

where $R^n f \to 0$ when $N \to \infty$ [11][12]. This describes the decomposition process.

3.2. Dictionary of Gabor functions

In the described IDS solution we proposed a waveform from a time-frequency dictionary can be expressed as translation (u), dilation (s) and modulation (ω) of a window function $g(t) \in L^2(R)$

$$g_\gamma(t) = \frac{1}{\sqrt{s}} g\left(\frac{t-u}{s}\right) e^{i\omega t}, \tag{7}$$

where

$$g(t) = \frac{1}{\sqrt{s}} e^{-\pi t^2}. \tag{8}$$

Optimal time-frequency resolution is obtained for Gaussian window $g(t)$, which for the analysis of real valued discrete signals gives a dictionary of Gabor functions

$$g_\gamma(x) = C(\gamma, \varphi) g\left(\frac{x-u}{s}\right) \sin\left(2\pi \frac{\omega}{N}(x-u) + \varphi\right), \tag{9}$$

where N is the size of the signal for which the dictionary is constructed. $C(\gamma, \varphi)$ is normalizing constant used achieve atom unit energy $\|g_\gamma\| = 1$ and $\gamma = \{s, u, \omega, \varphi\}$ denotes parameters of the dictionary's functions [16][17].

We implemented the dictionary originally by Mallat and Zhang in [11], the parameters of the atoms are chosen from dyadic sequences of integers. Scale s, which corresponds to an atom's width in time, is derived from the dyadic sequence $s = 2^j, 0 < j < L$ (signal size $K = 2^L$ and j is octave). Parameters u and ω, which correspond to an atom's position in time and frequency, are sampled for each octave j with interval $s = 2^j$.

In order to create an overcomplete set of Gabor functions, dictionary D was built by varying subsequence atom parameters: scale (s), translation (u), modulation (ω) and phase (φ). Base functions dictionary D was created with using 10 different scales and 50 different modulations. In Figure 2 example atoms from dictionary D are presented.

3.3. Search in the dictionary of atoms

In basic Matching Pursuit algorithm atoms are selected in every step from entire dictionary which has flat structure. In this case algorithm causes significant processor burden. In our coder dictionary with internal structure was used Fig. 2.
Dictionary is built from:

- Atoms,
- Centered atoms.

Centered atoms groups such atoms from D that are as much correlated as possible to each other. To calculate measure of correlation between atoms, function $o(a, b)$ can be used [15] :

$$\boldsymbol{o(a,b)} = \sqrt{\mathbf{1} - \left(\frac{|\langle \boldsymbol{a},\boldsymbol{b}\rangle|}{\|\boldsymbol{a}\|_2 \|\boldsymbol{b}\|_2}\right)^2}. \tag{10}$$

The quality of centered atom can be estimated according to (9):

$$\boldsymbol{O_{k,l}} = \frac{\mathbf{1}}{|\boldsymbol{LP_{k,l}}|} \sum\nolimits_{\boldsymbol{i} \in \boldsymbol{LP_{k,l}}} \boldsymbol{o}\left(\boldsymbol{A_{c(i)}}, \boldsymbol{W_{c(k,l)}}\right), \tag{11}$$

where $LP_{k,l}$ is a list of atoms grouped by centered atom. $O_{k,l}$ is a mean of local distances from centered atom $W_{c(k,l)}$ to the atoms $A_{c(i)}$ which are strongly correlated with $A_{c(i)}$. Centroid $W_{c(k,l)}$ represents atoms $A_{c(i)}$ which belongs to the set $i \in LP_{k,l}$. List of atoms $LP_{k,l}$ should be selected according to the equation (12):

$$\mathbf{max}_{i \epsilon LP_{k,l}} \, o\left(A_{c(i)}, W_{c(k,l)}\right) \leq \mathbf{min}_{j \in D \setminus LP_{k,l}} \, o\left(A_{c(j)}, W_{c(k,l)}\right). \tag{12}$$

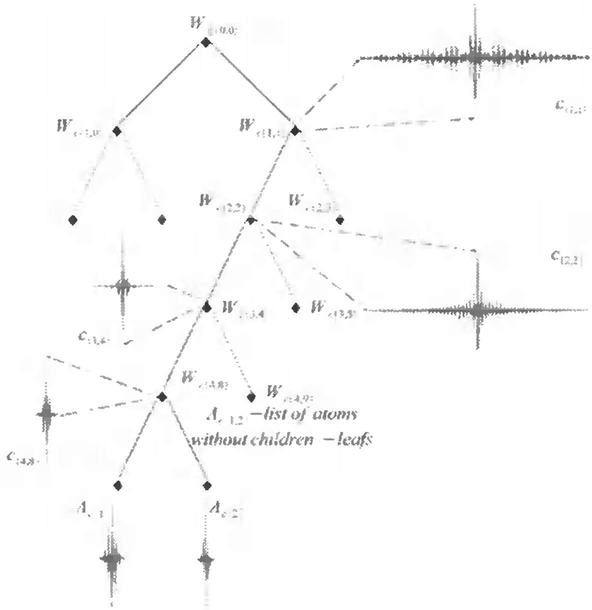

Fig. 2. Base functions dictionary structure.

4. EXPERIMENTAL RESULTS

We modified algorithm [15] in order to improve the input signal approximation. Instead of calculating projection during creation tree structure of Base Function Dictionary-BFD we used cross correlation as a measure of similarity between different atoms a and b in atoms set.

Cross-correlation can be calculated according to equation (13):

$$R_{a,b}(t) = \sum_{m=-\infty}^{\infty} a^{*}(m) b(t+m), \tag{13}$$

where $R_{a,b}(t)$ – cross-correlation, a and b atoms from dictionary, a^{*} – conjugation of atom a, t – subsequent value of cross-correlation, m – index of atom values. Proposed algorithm modification allows us to improve process of creation tree structure BFD. As a result we achieve better input signal approximation Fig. 3.

The matching pursuits algorithm produces three important elements of information: the set of projection coefficients $\alpha = \{\alpha_0, \alpha_1, \ldots, \alpha_{n-1}\}$, the set of residues $Rf = \{R^0 f, R^1 f, \ldots, R^{n-1} f\}$ and the list of dictionary elements chosen to approximate of $f(x)$, represented as $g_\gamma = \{g_{\gamma_0}, g_{\gamma_1,\dots,} g_{\gamma_{n-1}}\}$. This three factors α, Rf and g_γ completely define the discrete signal $f(x)$.

The main steps of algorithm are presented in subsequent points:

1) Base functions and the tree structure dictionary calculation (off-line):
   a) generation of all base functions,
   b) calculation of cross-correlation between atoms,
   c) tree structure dictionary calculation with the use of k-means clustering algorithm:
      i. centroid calculation,
      ii. distance calculation between atoms and centroid,
      iii. setting up connections between nodes in the tree structure,
      iv. scalar product between atoms updates;
2) Atom search process in the tree structure dictionary (on-line process):
   a) calculate scalar products (with the use of FFT) of present network 1-D signal with root node's children,
   b) set position in the tree structure for the best children (with highest scalar product) of the root node,
   c) calculate scalar products (by means of projection operation) until leaf node of the tree structure is reached,
   d) store parameters (projection, index of atom in dictionary and signal residue) of the best leaf atom.

For anomaly detection classification we used two parameters:

- Matching Pursuit Mean Projection (MP-MP)

$$MP - MP = \frac{1}{n}\sum_{i=0}^{n-1} \alpha_i, \tag{14}$$

- Energies of coefficients, residues and dictionary elements

$$E_{(k)} = \left\|\alpha^{(k)}\right\|^2 + \left\|Rf^{(k)}\right\|^2 + \left\|g_\gamma^{(k)}\right\|^2. \tag{15}$$

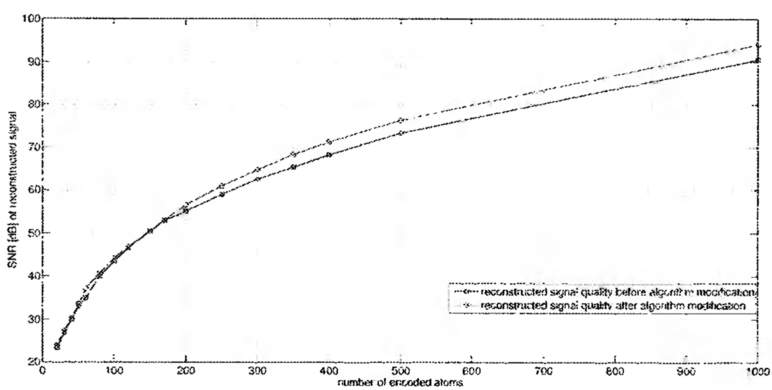

Fig. 3. Quality of reconstructed signal after algorithm modification.

In Tables 1-7 there are results for proposed ADS. Our system was tested with the use of public available benchmark test traces [20][21] and traces obtained from other sources [22].

Table 1. Detection Rate for W5D5 (FifthWeek, Day 5) [20] trace.

Network Traffic Feature	Total number of attack	Detected number of attack	Detection Rate [%]
ICMP flows/minute	68	50	73.52
ICMP in bytes/minute	68	57	83.82
ICMP out bytes/minute	68	55	80.88
ICMP in frames/minute	68	60	88.23
ICMP out frames/minute	68	57	83.82
TCP flows/minute	68	38	55.88
TCP in bytes/minute	68	42	61.76
TCP out bytes/minute	68	24	35.29
TCP in frames/minute	68	32	47.05
TCP out frames/minute	68	33	48.53
UDP flows/minute	68	67	98.53
UDP in bytes/minute	68	63	92.64
UDP out bytes/minute	68	61	89.70
UDP in frames/minute	68	63	92.53
UDP out frames/minute	68	61	89.70

Table 2. Cumulative DR – detection rate takes into consideration attacks recognized by all traffic features presented in Table 1. Results were compared to results achieved for fifth test week (Week5 Day1-5) of [20] traces.

Test Days	W5D1	W5D2	W5D3	W5D4	W5D5
DR [%] for all attack instances – DWT [19]	94.67	66.1	49.52	74.33	26.7
DR [%] for all attack instances MPMP (Matching Pursuit Mean Projection)	100	100	100	100	100
DR [%] attack types (DoS, U2R,R2L,PROBE) – DWT [19]	100	75	71.43	88.89	74.1
DR [%] attack types (DoS, U2R,R2L,PROBE) – MPMP (Matching Pursuit Mean Projection)	100	100	100	100	100

Table 3. Matching Pursuit Mean Projection - MP-MP for TCP trace with DDoS attacks (20 min. analysis window).

TCP trace (packet/second) CAIDA [22]	Window1 MPMP	Window2 MPMP	Window3 MPMP	MPMP for trace	MPMP for normal trace
Backscatter 2008.11.15	147.64	**414.86**	**368.25**	315.35	155.76
Backscatter 2008.08.20	**209.56**	162.38	154.75	157.38	155.76

Table 4. Matching Pursuit Energy parameter for TCP trace with DDoS attacks (20 min. analysis window).

TCP trace (packet/second) CAIDA [22]	Window1 $E_{(k)}$	Window2 $E_{(k)}$	Window3 $E_{(k)}$	$E_{(k)}$ for trace	$E_{(k)}$ for normal trace
Backscatter 2008.11.15	4.52e+7	**3.51e+8**	**2.16e+8**	2.01e+8	4.75e+7
Backscatter 2008.08.20	**9.54e+7**	4.27e+7	5.376e+7	6.76e+7	4.75e+7

Table 5. Matching Pursuit Mean Projection -MP-MP for TCP trace (20 min. analysis window).

TCP trace (packet/second) MAWI [21]	Window1 MPMP	Window2 MPMP	Window3 MPMP	MPMP for trace	MPMP for normal trace
Mawi 2004.03.06 tcp	214.32	177.81	300.11	248.01	242.00
Mawi 2004.03.13 tcp	279.11	216.23	217.65	238.33	242.00
Mawi 2004.03.20 tcp (attacked: Witty)	**321.54**	**367.45**	348.65	350.48	242.00
Mawi 2004.03.20 tcp (attacked: Slammer)	323.23	482.43	388.43	401.00	242.00

Table 6. Matching Pursuit Energy parameter - for TCP trace (20 min. analysis window).

TCP trace (packet/second) MAWI [21]	Window1 $E_{(k)}$	Window2 $E_{(k)}$	Window3 $E_{(k)}$	$E_{(k)}$ for trace	$E_{(k)}$ for normal trace
Mawi 2004.03.06 tcp	7.1e+7	7.52e+7	6.45e+7	7.23e+7	7.73e+7
Mawi 2004.03.13 tcp	8.56e+7	7.77e+7	8.54e+7	8.67e+7	7.73e+7
Mawi 2004.03.20 tcp (attacked: Witty)	**2.03e+8**	**1.46e+8**	**1.83e+8**	1.77e+8	7.73e+7
Mawi 2004.03.20 tcp (attacked: Slammer)	**3.34e+8**	**2.42e+8**	**3.4e+8**	3.34e+8	7.73e+7

Table 7. Proposed MP based ADS in comparison to DWT based ADS [19]. Both solutions were tested with the use of DARPA [20] tested (results in table are forWeek5 Day1 test day: DR-Detection Rate [%]. FP-False Positive [%]) for MP-MP and $E(k)$ energy parameter.

Traffic Feature	MP-MP DR[%]	MP-MP FP[%]	$E_{(k)}$ DR[%]	$E_{(k)}$ FP[%]	DWT DR[%]	DWT FP[%]
ICMP flows/minute	69.49	20.23	91.54	38.35	14.00	79.33
ICMP in bytes/minute	80.45	21.69	95.34	37.35	83.33	416.00
ICMP out bytes/minute	74.97	30.72	95.67	36.72	83.33	416.00
ICMP in frames/minute	79.08	28.76	85.98	35.24	32.00	112.00
ICMP out frames/minute	73.60	30.33	95.34	35.61	32.00	112.00
TCP flows/minute	89.54	35.56	98.95	38.72	26.67	74.67
TCP in bytes/minute	48.98	34.67	94.23	41.00	8.67	23.33
TCP out bytes/minute	81.22	28.34	96.67	34.24	6.67	36.00
TCP in frames/minute	37.98	26.11	96.98	36.09	2.00	36.00
TCP out frames/minute	39.55	28.34	96.78	34.24	2.00	74.67
UDP flows/minute	90.04	41.22	91.56	38.87	10.00	66.67
UDP in bytes/minute	99.63	42.19	99.73	46.34	11.33	66.67
UDP out bytes/minute	100.00	46.56	100	44.57	11.33	66.67
UDP in frames/minute	99.63	40.23	98.43	46.23	12.67	66.67
UDP out frames/minute	100.00	46.47	100	46.34	12.67	66.67

5. OVERALL DETECTION RATE

Overall detection rate is a measure of presented Anomaly Detection System performance. Overall Detection Rate – ODR is calculated for DR and FPR parameter. ODR takes into consideration set of traffic metrics where at the same time FPR is lowest and DR has highest value. ODR is also calculated for different ADS systems presented in [19, 10, 23, 25]. For presented system we obtain 97%-100% DR and 13-15% FPR for DARPA trace and DR = 94,20% FPR = 11,3% for all tested traces [20, 21, 22].

Table 8. Comparison of different methods of proposed ADS algorithm.

Publication	System algorithm	Network traces	DR [%]	FPR [%]	Comments
Presented ADS	MP	DARPA	97-100	13%-15	overall performance
Presented ADS	MP	all traces [20, 21, 22]	94.20	11,13	overall performance
Network Anomaly Detection Based on Wavelet Analysis [19]	DWT	DARPA	mean 23.37 overall 74.1-100	111.30	
Wavelet-based Detection of DoS Attacks [10]	CWT	DARPA + local campus network	94	24	overall performance
Non-Gaussian and Long Memory Statistical Characterizations for Internet Traffic with Anomalies [23]	statistic – LRD	campus network, artificial attacks	DDOS 40-96 FC 14-25	DDOS 20 FC 20	only DDOS or FC-Flash Crowd
Learning nonstationary models of normal network traffic for detecting novel attacks [24]	statistic – nonstationary models	DARPA	39	41	
Hybrid Intrusion Detection Systems (HIDS) using Fuzzy Logic [25]	fuzzy logic and data mining	DARPA + local network	69.6-98.4	24.70	
Hybrid Intrusion Detection with Weighted Signature Generation over Anomalous Internet Episodes [26]	SNORT 2.1 + ADS (data mining)	DARPA + campus network	60	30	
The Problem of False Alarms: Evaluation with Snort and DARPA 1999 Dataset [27]	SNORT 2.6 + preprocessors	DARPA	31.00	69.00	for SNORT IDS + preprocessors

- Network traffic feature: TCP byte in , ICMP flows: FPR = 13%, DR = 100%,
- Network traffic feature: TCP byte in, TCP flows: FPR = 15%, DR = 100%,
- Network traffic feature: TCP flows, UDP flows: FPR = 20%, DR = 100%.

It can be noticed that overall detection rate depends on set of network traffic features. Different sets of traffic features did not allow to achieve better DR and FPR.

6. CONCLUSIONS

In the article our developments in feature extraction for Intrusion Detection systems are presented. We showed that Matching Pursuit may be considered as very promising methodology which can be used in networks security framework. Upon experiments we may conclude that mean projection and energy parameter differs significantly for normal and attacked traces. Therefore, our system easily detects attacked traffic and triggers an alarm. The major contribution of this paper is a novel algorithm for detecting anomalies based on signal decomposition. In the classification/decision module we proposed to use developed matching pursuit features such as mean projection and energy parameter. We tested and evaluated the presented features and showed that experimental results proved the effectiveness of our method. We compared our solution to different ADS systems based on signal processing, data mining and hybrid algorithms.

BIBLIOGRAPHY

[1] Esposito M., Mazzariello C., Oliviero F., Romano S.P., Sansone C., 2005. Real Time Detection of Novel Attacks by Means of Data Mining Techniques. ICEIS (3) pp. 120-127.

[2] Davis G., Mallat S., Avellaneda M., 1997. Adaptive greedy approxima-tions, Journal of Constructive Approximation, vol. 13, pp.57-98.

[3] Esposito M., Mazzariello C., Oliviero F., Romano S.P., Sansone C., 2005. Evaluating Pattern Recognition Techniques in Intrusion Detection Systems. PRIS, pp. 144-153.

[4] FP7 INTERSECTION Project, Deliverable D.2.1: SOLUTIONS FOR SECURING HETEROGENEOUS NETWORKS: A STATE OF THE ART ANALYSIS.

[5] FP7 INTERSECTION (INfrastructure for heTErogeneous, Reislient, Secure, Complex, Tightly Inter-Operating Networks) Project Description of Work.

[6] Cheng C.-M., Kung H.T., Tan K.-S., 2002. Use of spectral analysis in defense against DoS attacks, IEEE GLOBECOM, pp. 2143-2148.

[7] Barford P., Kline J., Plonka D., Ron A. A signal analysis of network traffic anomalies, ACM SIGCOMM Internet Measurement Workshop 2002.

[8] Huang P., Feldmann A., Willinger W., 2001. A non-intrusive, wavelet-based approach to detecting network performance problems, ACM SIGCOMM Internet Measurement Workshop.

[9] Li L., Lee G., 2003. DDos attack detection and wavelets, IEEE ICCCN03, pp. 421--427.

[10] Dainotti A., Pescape A., Ventre G., 2006. Wavelet-based Detection of DoS Attacks, 2006 IEEE GLOBECOM, San Francisco (CA, USA).

[11] Mallat S., Zhang, 1993. Matching Pursuit with timefrequency dictonaries. IEEE Transactions on Signal Processing., vol. 41, no 12, pp. 3397-3415.
[12] Troop J.A., 2004. Greed is Good: Algorithmic Results for Sparse Appro-ximation. IEEE Transactions on Information Theory, vol. 50, no. 10.
[13] Tropp J.A., 2003. Greed is good: Algorithmic results for sparse approximation, ICES Report 03-04, The University of Texas at Austin.
[14] Gribonval R., 2001. Fast Matching Pursuit with a Multiscale Dictionary of Gaussian Chirps. IEEE Transactions on Signal Processing., vol. 49, no. 5.
[15] Jost P., Vandergheynst P., Frossard P., 2005. Tree-Based Pursuit: Algorithm and Properties. Swiss Federal Institute of Technology Lausanne (EPFL),Signal Processing Institute Technical Report.,TR-ITS-2005.013.
[16] Elad M., 2010. Sparse and Redundant Representations: From Theory to Applications in Signal and Image Processing, Springer.
[17] Gabor D., 1946. Theory of communication. Journal of Institution Electrical Engineering, vol. 93, no. 26, pp. 429-457.
[18] Janssen A., 1981. Gabor representation of generalized functions. Journal of the Mathematical. Analysis. and Applications, vol. 83, no. 2, pp. 377–394.
[19] Lu W., Ghorbani Ali A., 2009. Network Anomaly Detection Based on Wavelet Analysis, EURASIP Journal on Advances in Signal Processing, vol. 2009, Article ID 837601. doi:10.1155/2009/837601
[20] Defense Advanced Research Projects Agency DARPA Intrusion Detection Evaluation Data Set: http://www.ll.mit.edu/mission/communications/ist/corpora/ideval/data/index.html
[21] WIDE Project: MAWI Working Group Traffic Archive at tracer.csl.sony.co.jp/mawi/
[22] The CAIDA Dataset on the Witty Worm - March 19-24, 2004. Colleen Shanon and David Moore, www.caida.org/passive/witty.
[23] Scherrer A., Larrieu N., Owezarski P., Borgant P., Abry P., 2007. Non-Gaussian and Long Memory Statistical Characterizations for Internet Traffic with Anomalies. IEEE Transactions On Dependable and Secure Computing, vol. 4, no. 1, pp. 56-70.
[24] Mahoney M.V., Chan P.K., 2002. Learning nonstationary models of normal network traffic for detecting novel attacks, Proceedings of the Eighth ACM SIGKDD, pp. 376-385.
[25] Shanmugam B., Idris N.B., 2011. Hybrid Intrusion Detection Systems (HIDS) using Fuzzy Logic, Intrusion Detection Systems, InTech, pp. 135-154, http://www.intechopen.com/books/show/title/intrusion-detection-systems.
[26] Hwang K., Cai M., Chen Y., Qin M., 2007. Hybrid Intrusion Detection with Weighted Signature Generation over Anomalous Internet Episodes, IEEE Transactions on dependable and secure computing, vol. 4, no. 1, pp. 1-15.
[27] Tjhai G.C., Papadaki M., Furnell S.M., Clarke N.L., 2008. The Problem of False Alarms: Evaluation with Snort and DARPA 1999 Dataset, [in:] TrustBus 2008, LNCS 5185, Springer-Verlag, pp. 139-150.
[28] Choraś M., Saganowski Ł., Renk R., Hołubowicz W., 2011. Statistical and signal-based net-work traffic recognition for anomaly detection. Expert Systems. The Journal of Knowledge Engineering.
[29] Garcia-Teodoro P., Diaz-Verdejo J., Macia-Fernandez G., Vazquez E., 2009. Anomaly-based network intrusion detection: Techniques, systems and challenges, Computers and security, Elsevier, vol. 28, pp. 18-28.

WYKRYWANIE ANOMALII SIECIOWYCH NA PODSTAWIE ADAPTACYJNEJ APROKSYMACJI SYGNAŁU

Streszczenie

W artykule zaproponowany został System Detekcji Anomalii w ruchu sieciowym z wykorzystaniem algorytmu dopasowania kroczącego. Zaproponowane zostały kolejne modyfikacje omawianej metody. Wydajność zastosowanego algorytmu została przedstawiona z użyciem testowych ścieżek ruchu sieciowego. Przedstawiono również porównanie zaproponowanej metody do innych rozwiązań systemów detekcji anomalii opartych o algorytmy: przetwarzania sygnałów, statystyczne oraz hybrydowe.

Słowa kluczowe: detekcja anomalii, dopasowanie kroczące, adaptacyjna aproksymacja sygnału

UNIWERSYTET TECHNOLOGICZNO-PRZYRODNICZY
IM. JANA I JĘDRZEJA ŚNIADECKICH W BYDGOSZCZY
ZESZYTY NAUKOWE NR 260
TELEKOMUNKACJA I ELEKTRONIKA 15 (2011), 49-61

MRI IMAGE ANALYSIS IN PATIENTS WITH A TUMOR OF THE CENTRAL NERVOUS SYSTEM – AN ATTEMPT OF DEVELOPING A MANAGEMENT ALGORITHM

Maciej Śniegocki[1], Agnieszka Nowacka[2], Jacek Fisz[3]
Aleksandra Śniegocka[4], Marcin Buczkowski[5]

[1] Department of Neurotraumatology CM UMK
[2] Department of Neurosurgery and Neurotraumatology CM UMK
[3] Department of Computer Science and Methodology of Science Work CM UMK
[4] Department of Clinical Psychology CM UMK
University Hospital No. 1, ul. M. Skłodowskiej-Curie 9, 85-094 Bydgoszcz
[5] Department of Physics and Biophysics UWM,
Plac Cieszyński 1 (bl. 43), 10-726 Olsztyn

Summary: Magnetic resonance imaging study is currently the reference method for the detection and diagnosis of the central nervous system tumors. A large number of tumors, especially high-grade, has a higher water content in the cells, which results in prolongation of MRI T1 and T2 what appearance as increased signal intensity in in T2-weighted images and the reduction in T1-weighted images. MRI can be performed with administration of contrast agent, which shortens T1 and increases signal on T1-weighted sequences. This allows to identify areas of increased angiogenesis), which is the exponent of the cancer malignancy degree and its biological activity. Obtained MRI images are analyzed and evaluated by a radiologist and a clinician. Most of the time it is the "by the eye" analysis, which is based on the MRI image evaluation by the generally accepted radiological standards. However, this method is relatively inaccurate, which in turn can bring to the wrong diagnosis of the disease and implementation or even lack of implementation of appropriate treatment. More and more researches are conducted in this area, but developed methods are usually very complicated and difficult to carry out by the "layman" which is the clinician. That is why the attempt is made, to develop a simple and clear algorithm for MRI image analysis in patients with the central nervous system tumors, allowing for quick and objective evaluation of magnetic resonance imaging study.

Keywords: tumor, MRI image, angiogenesis, image analysis

1. TUMORS OF THE CENTRAL NERVOUS SYSTEM

Central nervous system tumors are approximately 1.5% of all cancers occurring in the human body, but their incidence is still increasing. Globally, the incidence of deaths due to intracranial tumors is estimated to be approximately 2.3% of all deaths due to cancer. 70-75% of them are primary tumors, and 20-25% are metastatic tumors. Due to the specific structure and functions of the brain, central nervous system tumors differ significantly from tumors located in other parts of the body. The very location of the tumor, regardless of its growth and malignancy, affects on the prognosis and patient's functional status. In case of location of the lesion in the area of important vital structures, both a tumor growth and its surgical treatment is a huge risk of severe disability or death of the patient.

Tumors of the central nervous system can be classified according to several basic criteria. The first one is the presentation of tumors due to their location within the cranial cavity. There are supratentorial tumors (located in the lobes of the brain, in deep structures of the telencephalon and diencephalon), which are 80-85% of all intracranial tumors in adults, and 40% in children, and infratentorial tumors (located within the cerebellum, brainstem, or the cerebellopontine angle), representing 15-20% of intracranial tumors in adults and 60% in children. This division is based on images obtained in radiological examinations, such as conventional radiography (X-ray), computed tomography (CT), magnetic resonance imaging (MRI) or positron emission tomography (PET). It is widely used in clinical practice, mainly because the location of the pathology is responsible for the occurrence of specific neurological symptoms, and allows to determine the quality of possible damage of the central nervous system after the surgery. Another criterion of division of the central nervous system tumors is the origin of the tumor tissue, first introduced by the World Health Organization (WHO) in 1979. The latest, 2007, WHO classification accounts the current state of knowledge about the biology of cancer, intracellular regulatory pathways, disturbed in the process of oncogenesis, and aspects of the therapeutic methods prediction.

TUMORS OF NEUROEPITHELIAL TISSUE

Astrocytic tumours
Pilocytic astrocytoma
- Pilomyxoid astrocytoma

Subependymal giant cell astrocytoma
Pleomorphic xanthoastrocytoma
Diffuse astrocytoma
- Fibrillary astrocytoma
- Gemistocytic astrocytoma
- Protoplasmic astrocytoma

Anaplastic astrocytoma
Glioblastoma
- Giant cell glioblastoma
- Gliosarcoma

Gliomatosis cerebri

Oligodendroglial tumours
Oligodendroglioma
Anaplastic oligodendroglioma

Oligoastrocytic tumours
Oligoastrocytoma
Anaplastic oligoastrocytoma

Ependymal tumours
Subependymoma
Myxopapillary ependymoma
Ependymoma
- Cellular
- Papillary
- Clear cell
- Tanycytic

Anaplastic ependymoma

Choroid plexus tumours
Choroid plexus papilloma
Atypical choroid plexus papilloma
Choroid plexus carcinoma

Other neuroepithelial tumours
Astroblastoma
Choroid glioma of the third ventricle
Angiocentric glioma

Neuronal and mixed neuronal-glial tumours
Dysplastic gangliocytoma of cerebellum (Lhermitte-Duclos)
Desmoplastic infantile astrocytoma/ganglioglioma
Dysembryoplastic neuroepithelial tumour
Gangliocytoma
Ganglioglioma
Anaplastic ganglioglioma
Central neurocytoma
Extraventricular naurocytoma
Cerebellar liponeurocytoma
Papillary glioneuronal tumour [PGNT]
Rosette-forming glioneuronal tumour of the fourth ventricle
Paraganglioma

Tumours of the pineal region
Pineocytoma
Pineal parenchymal tumour of intermediate differentiation
Pineoblastoma
Papillary tumour of the pineal region [PTPR]

Embryonal tumours
Medulloblastoma
- Desmoplastic/nodular medulloblastoma
- Medulloblastoma with extensive nodularity
- Anaplastic medulloblastoma
- Large cell medulloblastoma

CNS primitive neuroectodermal tumour
- CNS Neuroblastoma
- CNS Ganglioneuroblastoma
- Medulloepithelioma
- Ependymoblastoma

Atypical teratoid/rhabdoid tumour

TUMOURS OF CRANIAL AND PARASPINAL NERVES

Schwannoma (neurilemoma, neurinoma)
- Cellular
- Plexiform
- Melanotic

Neurofibroma
- Plexiform

Perineurinoma
- Perineurinoma, NOS
- Malignant perineurinoma

Malignant peripheral nerve sheath tumour (MPNST)
- Epithelioid MPNST
- MPNST with mesenchymal differentiation
- Melanotic MPNST
- MPNST with glandular differentiation

TUMOURS OF THE MENINGES

Tumours of meningothelial cells
Meningioma
- Meningothelial
- Fibrous (fibroblastic)
- Transitional (mixed)
- Psammomatous
- Angiomatous
- Microcystic
- Secretory
- Lymphoplasmacyte-rich
- Metaplastic
- Chordoid
- Clear cell
- Atypical
- Papillary
- Rhabdoid
- Anaplastic (malignant)

Mesenchymal tumours
Lipoma
Angiolipoma
Hibernoma
Liposarcoma
Solitary fibrous tumour
Fibrosarcoma
Malignant fibrous histiocytoma
Leiomyoma
Leiomyosarcoma
Rhabdomyoma
Rhabdomyosarcoma
Chondroma
Chondrosarcoma
Osteoma
Osteosarcoma
Osteochondroma
Haemangioma
Epithelioid haemangioendothelioma
Haemangiopericytoma
Anaplastic haemangiopericytoma
Angiosarcoma
Kaposi sarcoma
Ewing sarcoma (PNET)

Primary melanocytic lesions
Diffuse melanocytosis
Melanocytoma
Malignant melanoma
Meningeal melanomatosis

Other neoplasms related to the meninges
Haemangioblastoma

LYMPHOMAS AND HAEMATOPOIETIC NEOPLASMS

Malignant lymphomas
Plasmocytoma
Granulocytic sarcoma

GERM CELL TUMOURS

Germinoma
Embryonal carcinoma
Yolk sac tumour
Choriocarcinoma
Teratoma
- Mature
- Immature
- Teratoma with malignant transformation

Mixed germ cell tumour

TUMOURS OF THE SELLAR REGION

Craniopharyngioma
- Adamantinomatous
- Papillary

Granular cell tumour
Pituicytoma
Spindle cell oncocytoma of the adenohypophysis

METASTATIC TUMOURS

Fig. 1. Classification of the central nervous system tumors according to WHO, 2007.

This division is based on histological assessment of tumor cell types using conventional optical microscopy and cytogenetic studies. The third criterion of division of the central nervous system tumors, which is also complementary to the WHO classification, is the histological malignancy of the tumor (called grading). We can distinguish four degrees of malignancy:

Malignancy degree – grade	Tumor malignancy	Survival after surgical removal of the tumor	Features of microscopic structure
I	Benign	> 5 years or complete recovery	Differentiation of cells resembling normal tissue weaving
II	Relatively benign	3-5 years	High cell density
III	Relatively malignant	2-3 years	Features of II + high mitotic index
IV	Malignant	6-15 months	Features of II and III + vascular proliferation and/or necrosis

In clinical practice all criteria of subdivision are taken into account. This allows the selection of appropriate therapy and assessing prognosis for patient survival.

2. CHARACTERISTICS OF THE MOST COMMON CENTRAL NERVOUS SYSTEM TUMORS

Glial tumors are the largest group of primary intracranial tumors. They represent about 45% of all brain tumors. Most of them occur in the 5th and 6th decade of life. They are neuroepithelial origin tumors, derived from precursors of glial cells. Among them we can distinguish: astrocytomas – the most frequent, oliodendrogliomas and ependymomas. There is a huge diversity and multiplicity of glial tumors histopathological types. From a practical point of view, it can be divided into low-grade gliomas (LGG), which include I and II grade tumors, according to WHO, as well as high-grade gliomas (HGG), to which include III and IV grade tumors, according to WHO.

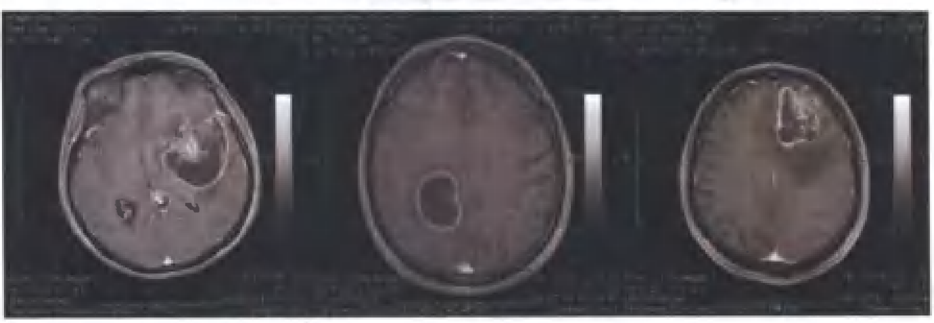

Fig. 2. MRI images. T1 + contrast, axial view. From left: astrocytoma anaplasticum WHO III, oligodendroglioma anaplasticum WHO III, glioblastoma multiforme WHO IV.

LGG grow slower than HGG and they can undergo a blast transformation to grade IV WHO into a glioblastoma multiforme (GBM), which is the most malignant form of astrocytoma, and the most common glial tumor. Glioblastoma has an invasive pattern of growth. Most of the time it occurs supratentorially within hemispheres of the brain, less infratentorially in the brainstem. The prognosis for patients with glioblastoma multiforme is very bad. Median survival ranges from 6 to 12 months.

Meningiomas are the most common primary intracranial tumors of low grade malignancy. They represent about 18% of all central nervous system tumors. They come from meningothelial cells (meningeal space cells). They create a wide attachment with the dura mater. They can grow into a skull and soft tissues of the head layers. They grow slowly and do not infiltrate the surrounding tissues, but only oppress and move the brain. Their slow growth allows adaptation of the brain in relation to increasing oppressor masses, so they may attain considerable size before a symptoms of a focal damage to the central nervous system appear in a patient. Mostly their location is parasagittal, convexity, tubercullum sellae, sphenoidal ridge, olfactory groove and falx; less is lateral ventricle, tentorial, middle fossa, orbital, intrasylvian and extracalvarial.

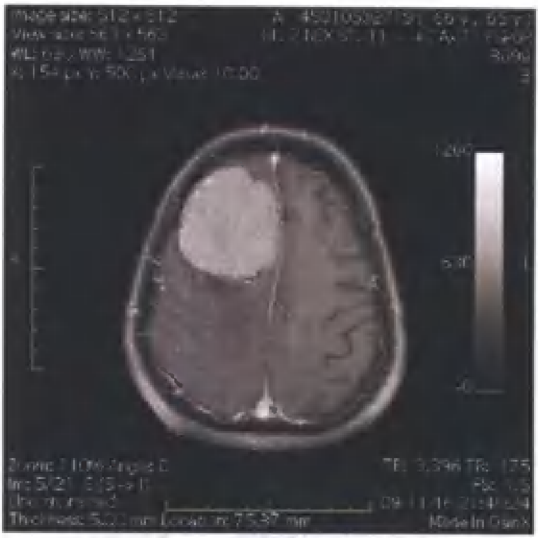

Fig. 3. MRI images. T1 + contrast, axial view. Meningioma meningotheliale WHO I.

Metastatic tumors almost ten times exceed the number of all primary central nervous system tumors. The most common primary source of metastasis is lung cancer (about 50%), especially small cell carcinoma and adenocarcinoma. Other causes include breast cancer, kidney, colon and rectum, and melanoma. In about 30-40% of metastases to the central nervous system occur singly. But more often multiple changes are observed. They are the most characteristic for malignant melanoma and lung cancer. Metastatic tumors are localized mostly within the cerebral hemispheres (80%), on the border of gray and white matter with a predilection for the parietal lobe, less in the cerebellar hemispheres (16%) and in the brainstem (4%). Some cancers, such as uterine cancer, colorectal cancer or small cell lung cancer, show a predilection for infratentorial metastasis formation. Metastatic tumors, in addition to cortico-subcortical location, are characterized by relatively large swelling of the brain tissues sourrounding the tumor, which affects the symptoms of increased intracranial pressure or focal damage to the central nervous system.

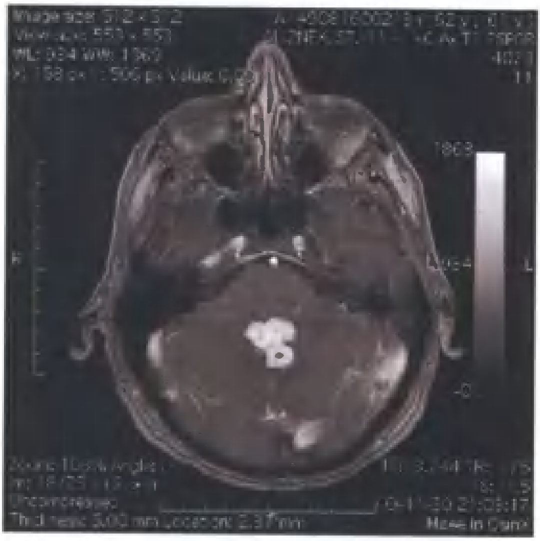

Fig. 4. MRI images, T1 + contrast, axial view. Carcinoma metastaticum cerebri.

3. IMAGING METHODS OF THE CENTRAL NERVOUS SYSTEM TUMORS

Currently, in case of the central nervous system tumor suspection, the most performed imaging examinations are computed tomography (CT) and magnetic resonance imaging (MRI).

Computed tomography to reconstruct the internal spatial structure of the object uses data on the absorption of ionizing radiation through the test object. On the basis of CT screening, a mass effect and/or reduced area density, you can eject the suspected presence of neoplasm in the central nervous system. The examination can be performed with or without contrast administration, which allows visualization of blood vessels and the degree of tissue perfusion. Depending on the histopathological type and the presence of calcification, tumors may be hypo-, normo-and hiperdensive in relation to the surrounding tissues. Many changes in the central nervous system cancer may be accompanied by swelling, resulting from the abolition of blood-brain barrier, shown on CT as an area of reduced density. Tumors such as meningiomas may grow into bones of the skull, causing erosion or hiperosteosis that are very well visible on the CT bone window. Computed tomography is also useful in the detection of calcifications and bleeding into the tumor masses, which often occurs in glioblastoma multiforme.

Significantly higher sensitivity and specificity, compared to CT scanning, shows a magnetic resonance imaging study. It is currently the reference method for the detection and diagnosis of the central nervous system tumors. The MRI uses the physical properties of hydrogen atoms, which placed in a strong magnetic field rearranges relatively to the magnetic field lines. Then they are stimulated by the resonant frequent electromagnetic pulses. During the stimulation decay, occurs an emission of a radio frequency waves. Received signals differ by intensity, depending on the type of tissue from which they originate. A large number of tumors, especially high-grade, has a higher water content in the cells, which results in prolongation of MRI T1 and T2 what appearace as increased signal intensity in in T2-weighted images and the reduction in T1-weighted images.

Table 2. Type of MRI signal in the case of selected central nervous system tumors.

Tumor histological type	T1 – weighted images	T2 – weighted images
Low grade gliomas	hipo/-izointensive	hiperintensive
High grade gliomas	hipo/-izointensive	hiperintensive
Meningiomas	iso-/hipointensive	iso-/hipointensive
Metastatic tumors	hipo/-izointensive	hiperintensive

As with CT, MRI can be performed without or with administration of contrast agent (usually gadolinium), which shorten T1 and increase signal on T1-weighted sequences. This allows to identify areas of increased blood flow (increased angiogenesis). Increased angiogenesis, the formation of blood vessels in tumor tissues, is the exponent of the cancer malignancy degree and its biological activity. Microcirculation can be illustrated by examination of brain tissue perfusion (eg. PWI MRI – weighted perfusion MRI, DCE MRI - dynamic contrast enchanced MRI). Administration of the contrast agent can also detect damage to the blood-brain barrier and allows to find the boundary between tumor and surrounding edema. The degree of after-contrast signal increasement depends on the concentration of contrast agent and magnetic fields force.

There are many MRI sequences and techniques, eg. FLAIR – fluid attenuated inversion recovery, STIR – short tau inversion recovery, MRA – magnetic resonance angiography, DWI – difussion weighted imaging, MRS – magnetic resonance spectroscopy, DTT MRI – difussion tensor tractography MRI. This an examination highly exceed computed tomography in the diagnosis of tumors of the central nervous system. Of course it has its limitations, such as the relatively long examinating time, sensitivity to motion artifacts, lack of examination possibility in case of the metal presence in patient's body, and the high price of examination. Despite that, it has many advantages, that put it in the first place in neuroimaging diagnosis, including:

- the possibility of obtaining images in any plane, which allows to define a very precise topographical relationships in relation to adjacent anatomical structures,
- high contrast resolution between imaging tissues,
- lack of bone artifacts,
- greater sensitivity than CT,
- possibility to conduct the examination in pregnant women (very low risk of adverse effects on the fetus of the magnetic field, as opposed to harmful ionizing radiation X in the case of CT),
- non-invasive examination,
- repeatability of examination.

4. CLASSICAL MRI IMAGINE ANALYSIS

After the MRI examination, obtained images are analyzed and evaluated by a radiologist and a clinician. Most of the time it is the "by the eye" analysis. It is based on the MRI image evaluation by the generally accepted radiological standards. However, this method is relatively inaccurate. This is influenced by many factors, such as:

- High evaluation subjectivity,
- influence of the experience of the image evaluator,
- influence of the fatigue of the image evaluator,
- low reproducibility of the analysis results.

These factors make the obtained MRI images to be evaluated in an improper manner, sometimes with very frivolous reasons, which in turn can bring to the wrong diagnosis of the disease and implementation or even lack of implementation of appropriate treatment. For this reason, the best solution would be to introduce a computerized algorithm used to evaluate the MRI. More and more researches are conducted in this area, but developed methods are usually very complicated and difficult to carry out by the "layman" which is the clinician. That is why the attempt is made, to develop a simple and clear algorithm for MRI image analysis in patients with the central nervous system tumors, allowing for quick and objective evaluation of magnetic resonance imaging study.

5. HOW TO DO IT – A NEW METHOD

In a patient with suspicion of a central nervous system tumor, a magnetic resonance imaging with the administration of contrast agent (gadolinium) is performed. The first sequences are performed without a contrast agent, and then the same sequences are performed immediately after administration of gadolinium. To comparement the T1-weighted (T1) and T1 + contrast (T1 + c) sequences are used. Images of the tumor, originating from the same imaging plane and the same cross section, have to be selected. On both images we denote the ROI (region of interest), which in this case is the tumor area.

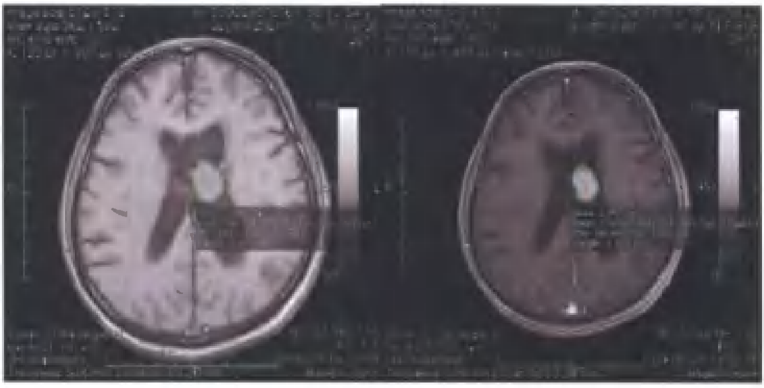

Fig. 5. MRI images, axial view, with denoted ROI's, from left T1 (ROI area), T1+c (ROI+c area).

The next step is to copy the ROI of the image and paste it in place of the brain that is not occupied by a cancer. This area will be the reference area for ROI. The received images undergo segmentation using DPM method (Dirichlet Process Mixture) of statistical computing environment R, which divides the image to the appropriate number of clusters.

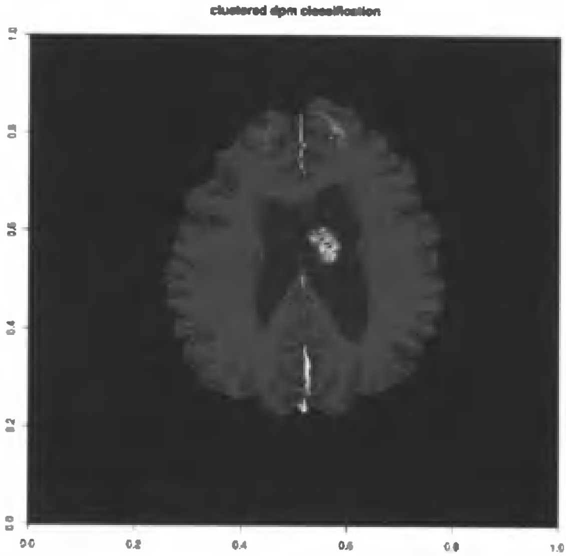

Fig. 6. MRI imagine after the DPM method segmentation.

From each of images (from ROI and the reference area) the number of pixels in the shade of gray scale (gray index) is automatically counted, and the results are presented in the form of histograms and tables.

Subsequently, the results of ROI and ROI + c for the image of the cross section of the site are subtracted from each other, and thus we obtain the measure as the ROI difference before and after administration of contrast. This difference reflects the amount of contrast agent, located in tumor microvessels, and thus indicates the thereof amount. As it is reported by previous research on the central nervous system tumors, the number of microvessels in the tumor mass correlates positively with the degree of malignancy, and therefore on the basis on so obtained results, it can be assessed with high probability which type of tumor do we have, which will allow a more accurate selection of treatment and assessment of prognosis.

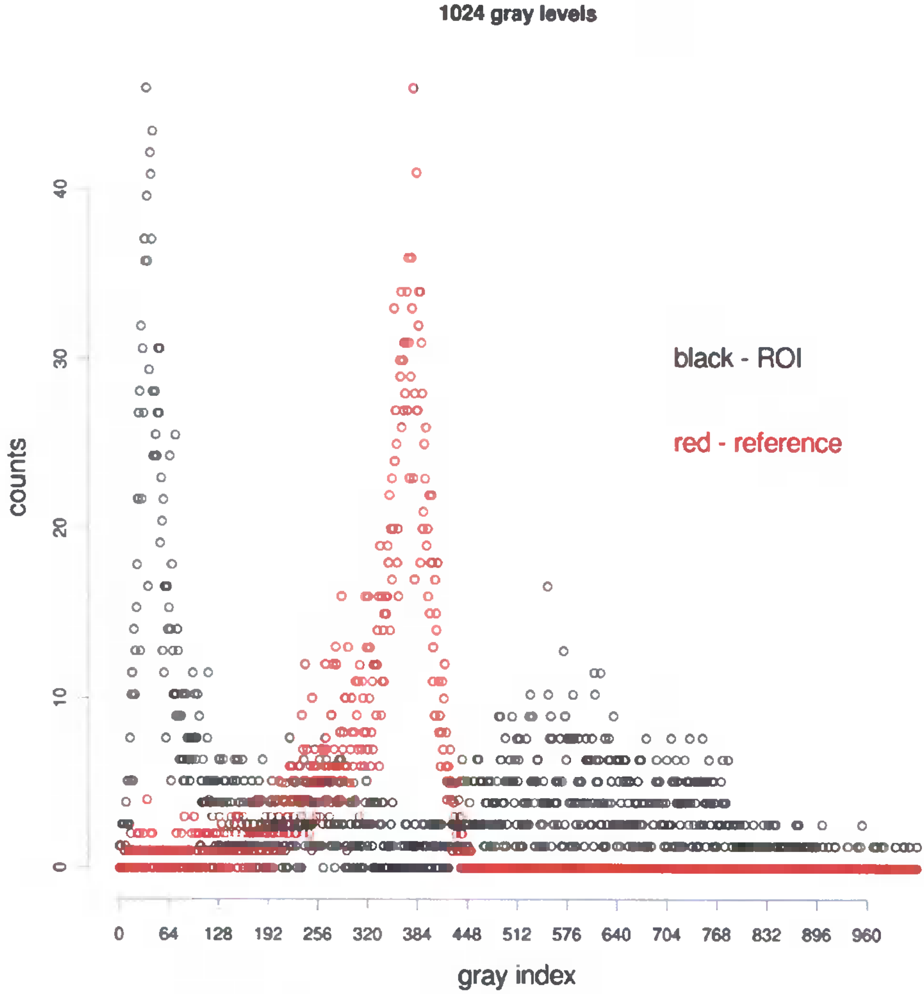

Fig. 7. A histogram showing the number of pixels in a shade of gray scale. On the y the number of pixels is indicated, and on the x the number corresponding shade of approved gray scale (from 0 to 1025). Black area shows the ROI analysis, and the red area the reference analysis.

6. RESULTS

In contrast to classical methods MRI image analysis in patients with the central nervous system tumors, the method presented by us can be a much more valuable tool for evaluation of magnetic resonance imaging studies, primarily due to:

- assessment automation,
- assessment repeatability,
- more objective assessment.

Excluded are all factors associated with human error, such as subjectivity, the impact of fatigue and experience, which greatly affect on the analysis quality reduction.

The new method can help to facilitate the work of both radiologists – the assessment of MRI images, and clinicians – when planning treatment, monitoring the disease and predicting prognosis for patient survival. Due to its simplicity and fast, direct obtaining of concrete results, it can also be used by those less experienced in the analysis of magnetic resonance images.

BIBLIOGRAPHY

[1] Aksoy F.G., Lev M.H., 2000. Dynamic Contrast – Enhanced Brain Perfusion Imaging: Technique and Clinical Applications. Sem Ultrasound CT MRI, 21 (6), pp. 462-477.

[2] Al-Okaili R.N., Krejza J., Woo J.H., Wolf R.L., O'Rourke D.M., Judy K.D., Poptani H., Melhem E.R., 2007. Intraaxial brain masses: MR imaging–based diagnostic strategy – initial experience. Radiology 243, pp. 539-550.

[3] Aronen H.J., Gazit I.E., Louis D.N., Buchbinder B.R., Pardo F.S., Weisskoff R.M., Griffith R.H., Cosgrove G.R., Halpern E.F., Hochberg F.H., Rosen B.R., 1994. Cerebral Blood Volume Maps of Gliomas: Comparison with Tumor Grade and Histologic Findings. Radiology 191, pp. 41-51.

[4] Brem S., Cotran R., Folkman J., 1972. Tumor angiogenesis: a quantitative method for histologic grading. J Natl Cancer Inst 48, pp. 347-356.

[5] Emblem K.E., Zoellner F.G., Tennoe B., Nedregaard B., Nome T., Due-Tonnessen P., Hald J.K., Scheie D., Bjornerud A., 2008. Predictive modeling in glioma grading from MR perfusion images using support vector machines. Magn Reson Med 60, pp. 945-952.

[6] Folkman J., 1992. The role of angiogenesis in tumor growth. Semin Cancer Biol, 3, pp. 65-71.

[7] Folkman J., 1990. What is the evidence that tumors are angiogenesis dependent? J Natl Cancer Inst 82, pp. 4-6.

[8] Ginsberg L., Fuller G., Schomer D., Kau B.A., Kispert D.B., 1996. Does lack of enhancement of brain tumors on MR imaging correlate with low grade malignancy? A histopathologic study. [In:] Proceedings of the American Society of Neuroradiology, Seattle–Washington, pp. 32-33.

[9] Glotsos D., Tohka J., Ravazoula P., Cavouras D., Nikiforidis G., 2005. Automated diagnosis of brain tumors astrocytomas using probabilistic neural network clustering and support vector machines. Int J Neural Syst 15, pp. 1-11.

[10] Greenberg M.S., Arredonto N., 2010. Handbook of neurosurgery – 7th edition, Thieme.

[11] Higano S., Yun X., Kumabe T., Watanabe M., Mugikura S., Umetsu A., Sato A., Yamada T., Takahashi S., 2006. Malignant astrocytic tumors: clinical im- portance of apparent diffusion coefficient in prediction of grade and prognosis. Radiology 241, pp. 839-846.

[12] Huang Y., Lisboa P.J.G., El-Deredy W., 2003. Tumour grading from magnetic resonance spectroscopy: a comparison of feature extraction with variable selection. Stat Med 22, pp. 147-164.

[13] Knopp E.A., Cha S., Johnson G., Mazumdar A., Golfinos J.G., Zagzag D., Miller D.C., Kelly P.J., Kricheff I.I., 1999. Glial Neoplasms: Dynamic Contrast – Enhanced T2* – weighted MR Imaging. Radiology 211, pp. 791-798.

[14] Kremer S., Grand S., Remy C., Esteve F., Lefournier V., Pasquier B., Hoffmann D., Benabid A.L., Le Bas J.F., 2002. Cerebral blood volume mapping by MR imaging in the initial evaluation of brain tumors. J Neuroradiol 29, pp. 105-113.
[15] Law M., Cha S., Knopp E. A., Johnson G., Arnett J., Litt A.W., 2002. High–Grade Gliomas and Solitary metastases: Diffe – rentiation by Using Perfusion and Proton Spectroscopic MR Imaging. Radiology 222, pp. 715-721.
[16] Lev M.H., Hochberg F., 1998. Perfusion Magnetic Resonance Imaging to Assess Brain Tumor Responses to New Therapies. Cancer Control 5 (2), pp. 115-123.
[17] Lev M.H., Ozsunar Y., Henson J.W., Rasheed A.A., Barest G.D., Harsh G.R., Fitzek M.M., Chiocca E.A., Rabinov J.D., Csavoy A.N., Rosen B.R., Hochberg F.H., Schaefer P.W., Gonzalez R.G., 2004. Glial tumor grading and outcome prediction using dynamic spin-echo MR susceptibility mapping com- pared with conventional contrast-enhanced MR: confounding effect of elevated rCBV of oligodendrogliomas. Am J Neuroradiol 25, pp. 214-221.
[18] Liberski P.P., Kozubski W., Biernat W., Kordek R., 2011. Neuroonkologia kliniczna. Wyd. Czelej.
[19] Louis D.N., Ohgaki H., Wiestler O.D., Cavenee W.K., Burger P.C., Jouvet A., Scheithauer B.W., 2007. The 2007 WHO Classification of Tumours of the Central Nervous System. Springer-Verlag.
[20] Lüdemann L., Grieger W., Wurm R., Budzisch M., Hamm B., Zimmer C., 2001. Comparison of dynamic contrast–enhanced MRI with WHO tumor grading for gliomas. Eur Radiol 11, pp. 1231-1241.
[21] Majós C., Julià-Sapé M., Alonso J., Serrallonga M., Aguilera C., Acebes J.J., Arús C., Gili J., 2004. Brain tumor classification by proton MR spectroscopy: comparison of diagnostic accuracy at short and long TE. Am J Neuro-radiol 25, pp. 1696-1704.
[22] Melhem E.R., Davatzikos C., 2008. Multi-parametric tissue characterization of brain neoplasms and their recurrence using pattern classification of MR images. Acad Radiol 15, pp. 966-977.
[23] Østergaard L., Hochberg F.H., Rabinov J.D., Sorensen A.G., Lev M., Kim L., Weisskoff R.M., Gonzalez R.G., Gyldensted C., Rosen B.R., 1999. Early changes measured by magnetic resonance imaging in cerebral blood flow, blood volume, and blood–brain barrier permeability following dexamethasone treatment in patients with brain tumors. J Neurosurg 90, pp. 300-305.
[24] Principi M., Italiani M., Guiducci A., Aprile I., Muti M., Giulianelli G., Ottoviano P., 2003. Perfusion MRI in the evaluation of the relationship between tumour growth, necrosis and angiogenesis in glioblastomas and grade 1 meningiomas. Neuroradiology 45, pp. 205-211.
[25] Provenzale J.M., Mukundan S., Baroriak D.P., 2006. Diffusion-weighted and perfusion MR imaging for brain tumor characterization and assessment of treatment. Radiology 239, pp. 632-649.
[26] Provenzale J.M., Mukundan S., Baroriak D.P., 2006. Diffusion-weighted and perfusion MR imaging for brain tumor characterization and assessment of treatment response. Radiology 239, pp. 632-649.
[27] Provenzale J.M., Wang G.R., Brenner T., Petrella J.R., Sorensen A.G., 2002. Comparison of Permeability in High–Grade and Low–Grade Brain Tumors Using Dynamic Susceptibility Contrast MR Imaging. Am J Roentgenol 178, pp. 711-716.

[28] Roberts H.C., Roberts T.P.L., Brasch R.C., Dillon W.P., 2000. Quantitative measurement of microvascular permeability in human brain tumors achieved using dynamic contrast - enhanced MR imaging: correlation with histologic grade. Am J Neuroradiol 21, pp. 891-899.
[29] Roberts H.C., Roberts T.P.L., Lee T.Y., Dillon W.P., 2002. Dynamic Contrast – Enhanced CT of Human Brain Tumors: Quantitative Assessment of Blood Volume, Blood Flow, and Microvascular Permeability: Report of Two Cases. Am J Neuroradiol 23, pp. 828-832.
[30] Siegal T., Rubinstein R.I., Tzuk-Shina T., Gomori J.M., 1997. Utility of relative cerebral blood volume mapping derived from perfusion magnetic resonance imaging in the routine follow up of brain tumors. J Neurosurg 86, pp. 22-27.
[31] Smith S.M., Jenkinson M., Woolrich M.W., Beckmann C.F., Behrens T.E., Johansen-Berg H., Bannister P.R., De Luca M., Drobnjak I., Flitney D.E., Niazy R.K., Saunders J., Vickers J., Zhang Y., De Stefano N., Brady J.M., Matthews P.M., 2004. Advances in functional and structural MR image analysis and implementation as FSL. Neuroimage 23 (suppl 1).
[32] Sugahara T., Korogi Y., Kochi M., Ikushima I., Hirai T., Okuda T., Shigematsu Y., Liang L., Ge Y., Ushio Y., Takahashi M., 1998. Correlation of MR Imaging - Determinated Cerebral Blood Maps with Histologic and Angiographic Determination of Vascularity of Gliomas. Am J Roengenol 171, pp. 1479-1486.
[33] Walecki J., Chojnacka E., 2007. Diagnostyka obrazowa guzów wewnątrzczaszkowych – część I – guzy neuroepitelialne. Onkologia w praktyce klinicznej, tom 3, nr 4, pp. 177-197.
[34] Weber M.A., Zoubaa S., Schlieter M., Juttler E., Huttner H.B., Geletneky K., Ittrich C., Lichy M.P., Kroll A., Debus J., Giesel F.L., Hartmann M., Essig M., 2006. Diagnostic performance of spectroscopic and perfusion MRI for distinc- tion of brain tumors. Neurology 66, pp. 1899-1906.
[35] Young R.J., Knopp E.A., 2006. Brain MRI: tumor evaluation. J Magn Reson Imaging 24, pp. 709-724.
[36] Zacharaki E.I., Wang S., Chawla S., Wolf R., Melhem E.R., Davatzikos C., 2009. Classification of brain tumor type and grade using MRI texture and shape in a machine learning scheme. Magnetic Resonance in Medicine 62, pp. 1609-1618.
[37] Zimny A., Sąsiadek M., 2005. Badania perfuzyjne TK i MR – nowe narzędzie w diagnostyce guzów wewnątrzczaszkowych. Adv Clin Exp Med. 14; 3, pp. 583-592.

ANALIZA OBRAZU MRI U CHORYCH Z GUZEM OŚRODKOWEGO UKŁADU NERWOWEGO – PRÓBA OPRACOWANIA ALGORYTMU POSTĘPOWANIA

Streszczenie

Badanie metodą rezonansu magnetycznego jest aktualnie metodą referencyjną przy wykrywaniu i diagnozowaniu nowotworów centralnego układu nerwowego. Duża część nowotworów, zwłaszcza o wysokim stopniu złośliwości, charakteryzuje się większą zawartością wody w komórkach, co w badaniu MRI skutkuje wydłużeniem T1 i T2, uwidocznionym jako nasilenie sygnału w obrazach T2-zależnych oraz jego obniżeniem w obrazach T1-zależnych. MRI można przeprowadzić

z podaniem środka kontrastowego, co powoduje skrócenie czasu T1 i podniesienie sygnału w sekwencjach T1-zależnych. Pozwala to zidentyfikować obszary wzmożonej angiogenezy, która jest wykładnikiem stopnia złośliwości nowotworu oraz jego aktywności biologicznej. Otrzymane obrazy MRI są analizowane oraz oceniane przez radiologa, a następnie klinicystę. Najczęściej jest to analiza „na oko" i opiera się ona na ocenie obrazu MRI z ogólnie przyjętymi normami radiologicznymi. Jest to jednak metoda stosunkowo niedokładna, co sprawia, iż otrzymane obrazy MRI mogą zostać ocenione w sposób niewłaściwy, co z kolei może przyczynić się do postawienia złej diagnozy co do choroby pacjenta i wdrożenie lub wręcz brak wdrożenia odpowiedniego leczenia. Prowadzonych jest coraz więcej badań w zakresie wprowadzenia skomputeryzowanego algorytmu służącego do oceny badania MRI, jednak wypracowane metody są najczęściej bardzo skomplikowane i trudne do przeprowadzenia przez „laika" jakim jest klinicysta. Właśnie dlatego podjęta została próba opracowania w miarę prostego i czytelnego algorytmu analizy obrazu MRI u pacjentów z chorobą nowotworową centralnego układu nerwowego, która pozwoli na szybką i obiektywną ocenę badania rezonansu magnetycznego.

Słowa kluczowe: nowotwory, obrazowanie MRI, angiogeneza, analiza obrazu

ISSN 1899-0088